ARL-TR-8797 ● SEP 2019

DEVCOM ARMY RESEARCH LABORATORY

Aerodynamic Investigation of a Supersonic Bending Body Projectile with Shape Optimization

Justin L Paul, Joseph D Vasile, Jim DeSpirito, and Sidra I Silton

NOTICES

Disclaimers

The findings in this report are not to be construed as an official Department of the Army position unless so designated by other authorized documents.

Citation of manufacturer's or trade names does not constitute an official endorsement or approval of the use thereof.

Destroy this report when it is no longer needed. Do not return it to the originator.

ARL-TR-8797 ● SEP 2019

Aerodynamic Investigation of a Supersonic Bending Body Projectile with Shape Optimization

Justin L Paul, Joseph D Vasile, Jim DeSpirito, and Sidra I Silton
Weapons and Materials Research Directorate, CCDC Army Research Laboratory

REPORT DOCUMENTATION PAGE

Form Approved
OMB No. 0704-0188

1. REPORT DATE *(DD-MM-YYYY)*	2. REPORT TYPE	3. DATES COVERED (From - To)
September 2019	Technical Report	1 July 2017–1 August 2018

4. TITLE AND SUBTITLE
Aerodynamic Investigation of a Supersonic Bending Body Projectile with Shape Optimization

5a. CONTRACT NUMBER

5b. GRANT NUMBER

5c. PROGRAM ELEMENT NUMBER

6. AUTHOR(S)
Justin L Paul, Joseph D Vasile, Jim DeSpirito, and Sidra I Silton

5d. PROJECT NUMBER

5e. TASK NUMBER

5f. WORK UNIT NUMBER

7. PERFORMING ORGANIZATION NAME(S) AND ADDRESS(ES)
CCDC Army Research Laboratory
ATTN: FCDD-RLW-LE
Aberdeen Proving Ground, MD 21005-5001

8. PERFORMING ORGANIZATION REPORT NUMBER
ARL-TR-8797

9. SPONSORING/MONITORING AGENCY NAME(S) AND ADDRESS(ES)

10. SPONSOR/MONITOR'S ACRONYM(S)

11. SPONSOR/MONITOR'S REPORT NUMBER(S)

12. DISTRIBUTION/AVAILABILITY STATEMENT
Approved for public release; distribution is unlimited.

13. SUPPLEMENTARY NOTES

14. ABSTRACT
A Particle Swarm Optimization algorithm was implemented along with an Euler (inviscid) computational fluid dynamics code to determine both body bending angles and locations that separately optimized two parameters: lift-to-drag ratio at the trim angle of attack and pitching moment coefficient at 0° angle of attack. The Air Force Finner missile at a Mach number of 2 was used as the baseline configuration. As a constraint, only configurations that could reach a trimmed condition over the angle of attack range ($-10° < \alpha < 10°$) were considered valid. The performance of the Euler code was evaluated by modeling the baseline Air Force Finner and comparing with archival experimental data as well as previous high-fidelity, viscous simulations. The Euler code produced comparable solutions to the viscous solutions for multiple bending body configurations with superior efficiency. Implementation of the shape optimization resulted in convergence to a different configuration, but with similar lift-to-drag ratios and trim angles of attack, for each of the optimized parameters. A "bentness" angle was defined that had a similar value for both optimal configurations. The optimal bending body configurations produced significantly higher pitching moment increments and improved maneuverability potential over a generic canard-controlled configuration with a 10° canard deflection. A 34% increase in lift-to-drag ratio was achieved for the bending body configurations. Overall, the optimization routine proved to be an efficient tool for producing highly maneuverable aerodynamic designs.

15. SUBJECT TERMS
guided munitions, aerodynamics, computational fluid dynamics, Particle Swarm Optimization, articulating nose

16. SECURITY CLASSIFICATION OF:			17. LIMITATION OF ABSTRACT	18. NUMBER OF PAGES	19a. NAME OF RESPONSIBLE PERSON
a. REPORT	b. ABSTRACT	c. THIS PAGE			Justin L Paul
Unclassified	Unclassified	Unclassified	UU	71	19b. TELEPHONE NUMBER (Include area code) 410-306-0797

Contents

List of Figures iv

List of Tables vi

1. Introduction 1

2. Projectile Design 4

2.1 Bent Body Model Variant 4

2.2 Canard Configuration Variant 6

3. Methodology 7

3.1 RANS Flow Solver 7

3.2 Inviscid Flow Solver 10

3.3 Particle Swarm Optimization 14

4. Results and Discussion 17

4.1 Baseline Configuration 17

4.2 Initial Bent Body Configurations 21

4.3 Design Space Analysis 33

4.4 Particle Swarm Optimization Analysis 35

4.5 Optimized Bent Body Projectile Analysis 42

5. Summary and Conclusions 52

6. References 54

Nomenclature 60

List of Symbols, Abbreviations, and Acronyms 61

Distribution List 62

List of Figures

Fig. 1 AFF straight body configuration 4

Fig. 2 Bent body configuration of the AFF 5

Fig. 3 Imaginary triangle characterizing the "bentness" of a generic bent body 6

Fig. 4 Canard configuration of the AFF 7

Fig. 5 Global view of an MIME-generated computational mesh 9

Fig. 6 Detailed perspective of aft end surface mesh and cut planes generated by MIME 9

Fig. 7 Detailed perspective of boundary layer refinement generated by MIME 10

Fig. 8 Detailed perspective of a computational mesh with 40 projectile diameters (Test Case 3) 11

Fig. 9 Cp contours in wake of projectile for Test Case 1 (left), 2 (middle), and 3 (right) 13

Fig. 10 Computational mesh with a heavily refined density box in the wake of the projectile (left) and resulting wake flowfield (right) for Test Case 4 14

Fig. 11 Detailed perspective of a final computational mesh of a bent body projectile (Test Case 6) 14

Fig. 12 Examples of C_m vs. α and the polynomial fits for one projectile that does not achieve a trimmed condition, and another projectile that achieves a trimmed condition 16

Fig. 13 CD vs. α at Mach 2 for straight body configuration 17

Fig. 14 CL vs. α at Mach 2 for straight body configuration 18

Fig. 15 Cm vs. α at Mach 2 for straight body configuration 18

Fig. 16 Cp contours at Mach 2: $\alpha = 0°$ from Cart3D (left) and CFD^{++} (right) 19

Fig. 17 Cp contours at Mach 2, $\alpha = 8°$ from Cart3D (left) and CFD^{++} (right) 20

Fig. 18 Cp contours at Mach 3, $\alpha = 0°$ from Cart3D (left) and CFD^{++} (right) 20

Fig. 19 Cp contours at Mach 3, $\alpha = 8°$ from Cart3D (left) and CFD^{++} (right) 20

Fig. 20 CD vs. α at Mach 2 for population of bent body models 22

Fig. 21 CL vs. α at Mach 2 for population of bent body models 22

Fig. 22 Cm vs. α at Mach 2 for population of bent body models 23

Fig. 23 CD vs. α at Mach 3 for population of bent body models 23
Fig. 24 CL vs. α at Mach 3 for population of bent body models 24
Fig. 25 Cm vs. α at Mach 3 for population of bent body models 24
Fig. 26 Cm vs. α at Mach 2 for chosen subset of bent body models 25
Fig. 27 CD vs. α at Mach 3 for select bent body models 27
Fig. 28 CL vs. α at Mach 3 for bent body models 28
Fig. 29 *L/D* vs. α at Mach 3 for select bent body models 28
Fig. 30 Cm vs. α at Mach 3 for bent body models 29
Fig. 31 Cp contours at Mach 3: $\alpha = 0°$ from Cart3D (left) and CFD^{++} (right) for Model 2 29
Fig. 32 Cp contours at Mach 3: $\alpha = 8°$ from Cart3D (left) and CFD^{++} (right) for Model 2 30
Fig. 33 Cp contours at Mach 3: $\alpha = 0°$ from Cart3D (left) and CFD^{++} (right) for Model 3 30
Fig. 34 Cp contours at Mach 3: $\alpha = 8°$ from Cart3D (left) and CFD^{++} (right) for Model 3 31
Fig. 35 Cp contours at Mach 3: $\alpha = 0°$ from Cart3D (left) and CFD^{++} (right) for Model 4 31
Fig. 36 Cp contours at Mach 3: $\alpha = 8°$ from Cart3D (left) and CFD^{++} (right) for Model 4 32
Fig. 37 Cp contours at Mach 3: $\alpha = 0°$ from Cart3D (left) and CFD^{++} (right) for Model 5 32
Fig. 38 Cp contours at Mach 3: $\alpha = 8°$ from Cart3D (left) and CFD^{++} (right) for Model 5 33
Fig. 39 Plots of a) Cm, b) CL, and c) CD vs. α for entire design space at Mach 2 34
Fig. 40 Plot of *L/D* (left) and $Cm0$ (right) vs. θ for trimmed configurations at Mach 2 35
Fig. 41 Optimal L/D configuration 35
Fig. 42 Optimal $Cm0$ configuration 35
Fig. 43 Parameter probability histograms for maximum *L/D* from in-house PSO algorithm 38
Fig. 44 Parameter probability histograms for maximum *L/D* from MATLAB PSO algorithm 38
Fig. 45 Parameter probability histograms for maximum $Cm0$ at $\alpha = 0°$ from in-house PSO algorithm 39
Fig. 46 Parameter probability histograms for maximum $Cm0$ at $\alpha = 0°$ from MATLAB PSO algorithm 39

Fig. 47 *L/D* results probability histograms from in-house PSO algorithm (left) and MATLAB PSO algorithm (right) 41
Fig. 48 $Cm0$ results probability histograms from in-house PSO algorithm (left) and MATLAB PSO algorithm (right) 41
Fig. 49 Cm vs. α for optimal configurations and canard configurations at Mach 2 42
Fig. 50 C_L vs. α for optimal configurations and canard configurations at Mach 2 43
Fig. 51 C_D vs. α for optimal configurations and canard configurations at Mach 2 43
Fig. 52 *L/D* vs. α for optimal configurations and canard configurations at Mach 2 44
Fig. 53 C_m increment for canard configurations and optimal bent configuration 46
Fig. 54 C_L increment for canard configurations and optimal bent configuration 46
Fig. 55 C_D increment for canard configurations and optimal bent configuration 47
Fig. 56 Mach contours on symmetry plane and surface pressure coefficient contours of the a) optimal $Cm0$, b), optimal *L/D*, and c) and $\delta = 10°$ canard configurations at Mach 2 and $\alpha = 0°$ 49
Fig. 57 Mach contours on symmetry plane and surface pressure coefficient contours of the a) optimal $Cm0$, b) optimal *L/D*, and c) $\delta = 10°$ canard configurations at Mach 2 and respective trim angle of attack. 50

List of Tables

Table 1 Control parameters for selected configurations 5
Table 2 Optimization control parameter values 6
Table 3 Test case descriptions for mesh resolution study 12
Table 4 Aerodynamic coefficients for mesh resolution study simulated at Mach 2, $\alpha = 8°$ 13
Table 5 Optimal configurations 36
Table 6 Optimization study metrics for maximum *L/D* at trim condition from in-house PSO algorithm 36
Table 7 Optimization study metrics for maximum *L/D* at trim condition from MATLAB PSO algorithm 36
Table 8 Optimization study metrics for maximum $Cm0$ from in-house PSO algorithm 37

Table 9 Optimization study metrics for maximum $Cm0$ from MATLAB PSO algorithm 37

Table 10 Comparison of significant aerodynamic metrics between the optimal bent body configuration, the canard configurations and the baseline configuration 44

1. Introduction

Small-diameter gun-launched munitions with fast and aggressive maneuver capabilities are of great research interest in the ballistics' community. Specifically, there has been growing interest to improve the delivery of munitions to be more precise and accurate to minimize collateral damage and maximize lethal effects. One method that can potentially achieve the necessary aggressive maneuver capability is bending body technology.

Conventional maneuvering munitions rely on actuators such as canards, fins, reaction control jets, or thrust vector control to provide the control authority necessary to perform maneuvers. For canard control, two configurations have typically been considered for maneuver control and are continuing to be developed: 1) slowly rolling munitions equipped with a single plane of movable lifting surfaces[1–3] and 2) nonrolling munitions with dual plane, movable lifting surfaces.[4] Canards are proven to be effective for some missions and maneuvers but can be limited in aggressive maneuver capability. Bending body technology offers a form of morphing airframe technology that can provide another method for control.[5,6] The bending body concept may provide aggressive maneuver capability, which can be limited with conventional canards, as they are subject to loss of effectiveness at high angle of attack, α, due to stall. Additionally, the interference loads that occur on the tail fins due to the interaction of vortices shed from the canard tips have been shown to limit maneuverability or adversely affect control. Vortex–fin interaction continues to be an area of active research, as its understanding is critical to increasing the performance of the flight body.[7–19] However, there are concerns for the actual implementation of bending body technology. While the projectile would fly in a straight configuration for most of the flight envelope, there is a significant increase in C_D during the maneuvering phase of flight (i.e., when the projectile is bent) that decreases performance.[5,6] Additionally, the center of pressure of the projectile may shift significantly when bent, causing destabilization of the projectile.[5,6] It is important to address these issues because there are several other advantages to using bending body technology, such as no canard-induced aerodynamic issues due to trailing vortex–fin interference, structural integrity during launch, and volumetric constraints associated with launch platforms.[16,20,21]

Previous research on bending body technology has focused on deflecting just the nose section of the projectile at its base.[22–26] In the early 1980s, Thomson considered a deflectable nose concept, where the weapon forebody is angularly deflected about a suitable pivot point as a way to control a tube-launched weapon.[22,23] Through his analyses, Thomson found the deflectable nose does not perform well at subsonic speeds but is feasible in the supersonic regime. Landers

et al.[24] performed wind tunnel tests at Mach 3 and Mach 6 on a hypervelocity projectile with a deflectable nose, comparing pitch control effectiveness with a canard configuration of the same projectile. They found the projectile with the deflectable nose control reduced the forebody C_D from 5% to 13% at Mach 3 and 6, respectively, attributed to the elimination of the control surfaces. They also found the reduction in axial force was increased to 10% to 30% at trim conditions when both control types provide similar maneuverability. Interference effects were found on both the deflected-nose and canard-controlled noses, but at low α (<6°). Vaughn and Auman[25] demonstrated capability to model the same deflected-nose concept using an intermediate-design level code based on the same Cartesian-grid, Euler computational fluid dynamic (CFD) solver used in the current paper. Shoesmith et al.[26] performed CFD simulations using the parabolized Navier–Stokes equations of the same deflected-nose projectile and found the downstream flow was insensitive to the nose deflection, providing an opportunity to decouple responses of nose control and fin-mounted actuators. They also determined the estimated actuator loads could be met with current actuators. Youn and Silton[6] demonstrated multiple bends can increase the advantage in control authority but at the cost of increased C_D.

Finding the "optimum" shape for a bent-body configuration would enable the leveraging of the control authority bending body technology offers, while mitigating the cost of increased C_D. Our approach to this problem is to simulate a bent body design with CFD and evaluate the results for the best performance. To evaluate the results of the simulations, we implement an optimization method to select the bent body configuration that best suits our chosen objective functions. We want to use optimization because the complex interactions between the performance metrics make closed form evaluation and analysis impractical. The challenge with optimizing the bending body projectile is the highly dimensional, multimodal nature of the problem. Evolutionary programming is a powerful optimization technique that is widely applicable to scientific research and the engineering industry. As a subset of machine learning, evolutionary programming provides a robust approach to the difficult optimization task. Li et al.[27] demonstrated that evolutionary programming (genetic algorithms, particle swarm optimization algorithms, etc.) can be used for aerodynamically driven shape optimization. Many other researchers and scientists have demonstrated similar investigations.[28–30]

The evolutionary programming technique used in this investigation is a Particle Swarm Optimization (PSO) algorithm.[31] PSO is based on the theory of swarm intelligence. Swarm intelligence is the property of a system where the collective behavior of individual particles evaluated locally in their environment contribute to

coherent global patterns in the population.[32] A natural, real-world analogy to PSO would be a "swarm" of bees, a school of fish, or an army of ants. A PSO algorithm evolves multiple iterations of a population of particles where each "particle" is a solution to the problem or objective function.[31,33–37] The objective function characterizes what is being optimized. Particles that are found to solve the problem poorly are encouraged to change their identity, while those found to solve the problem well are discouraged to change their identity. The algorithm iterates until a convergence condition is met. Defining aspects of PSO algorithms include metaheuristic, stochastic, and conditionally global.[31,33–37] PSO algorithms are metaheuristic because they find practical solutions instead of exact or perfect solutions. They are stochastic because the algorithm invokes pseudorandom number generation to assist searching the design space. They are conditionally global depending on how the algorithm is constructed or parameterized. If the algorithm is not properly constructed or parameterized, there may not be enough "search effort" or diversity in the iterations to search all necessary aspects of the design space of the problem. This issue may result in optimized individuals finding local extrema instead of global extrema or no extrema at all.

The current numerical study extends the investigation of Youn and Silton[6] using the common US Air Force Finner (AFF) missile* geometry as the baseline configuration. The effect of the body hinge location as well as the nose and body bending angles of the aerodynamic performance are considered. The ability of the inviscid Cart3D CFD solver to efficiently predict the aerodynamic coefficients is evaluated by comparing with the results of a fully viscous, Reynolds-Averaged Navier–Stokes (RANS) CFD solver as well as previously obtained experimental results. After establishing the efficiency and accuracy of Cart3D to determine the aerodynamic coefficients of the bending body configuration, a PSO algorithm is used to optimize a bent body design of the AFF geometry. Two objective functions were studied with three swarm sizes for a total of six unique optimization studies. The first objective function sought to maximize *L/D* and the second sought to optimize C_{m_0} while also requiring that the configuration reach a stable, trim condition. Three swarm sizes were used to determine the optimal individuals as well as the veracity of the optimal configurations. The optimization studies were completed at Mach 2 across an angle-of-attack range of –10° to 10°. The aerodynamics of the optimal bent configuration were then studied in greater detail and compared with conventional canard configurations.

* The term "projectile" is used in this report because our primary focus is a gun-launched guided munition, but it is aerodynamically equivalent to a missile.

2. Projectile Design

The numerical studies were completed using the basic AFF (D = 30 mm)[38–44] as the baseline geometry (Fig. 1). This projectile was chosen because it is a baseline supersonic geometry that has been studied extensively with a large volume of computational and empirical data available for comparison. The projectile has four uncanted, clipped delta tail fins spaced equidistant circumferentially. The AFF has a length-to-diameter, or fineness, ratio of 10 and the nose cone length is 2.5 D. The center of gravity, *c.g.,* is located at 4.8 D from the tip of the nose. The fins are beveled on the leading and trailing edges with a root cord of 4/3 D and a semi-span of 0.5 D. The baseline straight body configuration is shown in Fig. 1.

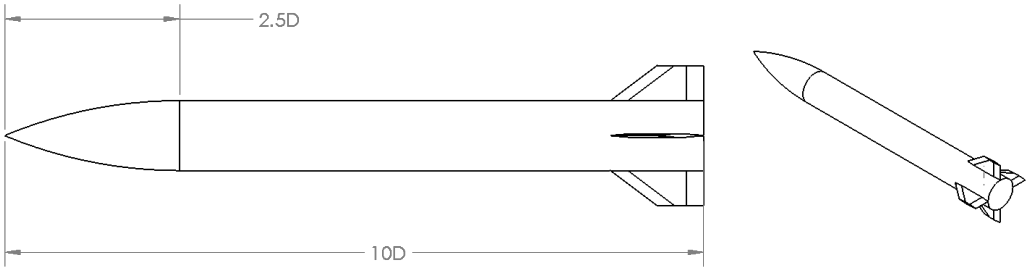

Fig. 1 AFF straight body configuration

2.1 Bent Body Model Variant

The projectile, in concept, is designed to fly in the baseline straight body configuration and morph into a bent body configuration when a maneuver is desired. A generic bent body configuration is shown in Fig. 2 with control parameters Φ_1, Φ_2, and Q_1. The first bend angle (Φ_1) is the angle between the projectile axis in the unbent configuration and the axis of the deflected forward-body section. The second bend angle (Φ_2) is the angle between the axis of the deflected forward-body section and the axis of the projectile nose section (or ogive). The first bend is located between the projectile's *c.g.* and the base of the nose cone (Q_1). Angle of attack, α, of the projectile is defined as the angle between the freestream velocity vector and the axis of the unbent portion of the projectile (dashed blue line in Fig. 2).

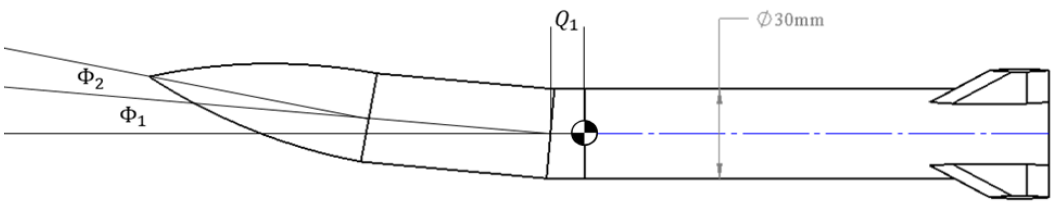

Fig. 2 Bent body configuration of the AFF

During the initial bent-body viability study, 31 configurations—30 randomly generated bent body configurations and the baseline configuration—were investigated. Q_1 was allowed to vary between 1 and 66 mm from the *c.g.* in 4.33-mm increments. The bend angles (Φ_1 and Φ_2) were initially permitted to vary from 0° to 7.5° in 0.5° increments. As the research progressed to the aerodynamic performance study using the Euler code, five configurations were chosen for comparison. The control parameters for these models are listed in Table 1. After the aerodynamic performance study, it was decided to reduce the size of the design space by doubling the value of the parameter increments (also eliminating the final option for each parameter) for the subsequent optimization studies. The new reduced design space is tabulated in Table 2.

Table 1 Control parameters for selected configurations

Model	Φ_1 (°)	Φ_2 (°)	Q_1 (mm)	Individual visualization
Straight body	0	0	*	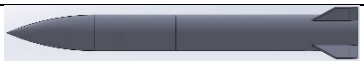
Model 2	0.5	6.5	68.75	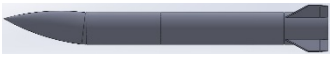
Model 3	3	3.5	10.25	
Model 4	5	4	1.25	
Model 5	1	0.5	23.75	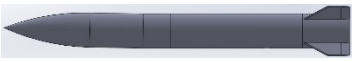

* Q_1 can take on any value in parameter space (Table 2) for straight body configuration.

Table 2 Optimization control parameter values

Φ_1 (°)	Φ_2 (°)	Q_1 (mm)
0	0	1.00
1	1	9.67
2	2	18.33
3	3	27.00
4	4	35.67
5	5	44.33
6	6	53.00
7	7	61.67

To effectively categorize the various geometries within the design space set by the bending body parameters, each particle is mapped onto an H versus θ characterization. An example of the imaginary triangle having the θ and H is modeled on the basic AFF in Fig. 3, where H represents the hypotenuse of the imaginary triangle and θ represents the angle between the straight body axis and the straight line from the center of gravity to the tip of the nose of the projectile. The H dimension only decreases 1.2 mm (0.4%) as the nose changes from the undeflected to the most deflected position. Therefore, the angle θ alone provides a good representation of the effective "bentness" to describe combined bending of the nose and body sections.

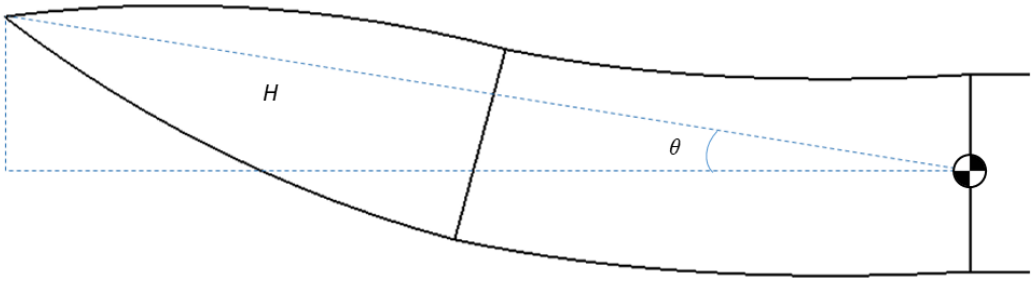

Fig. 3 Imaginary triangle characterizing the "bentness" of a generic bent body

2.2 Canard Configuration Variant

A generic canard configuration is shown in Fig. 4. The axial location and size of the canards were determined using Missile DATCOM[45] such that maximum control authority could be achieved without compromising stability in the Mach number regime of interest. Missile DATCOM is an aero-prediction code that uses a hybrid of empirical and analytical techniques to calculate aerodynamic coefficients. Four clipped-delta planform canards were placed in the "+" orientation (i.e., aligned with

the pitch and yaw axes) on the ogive section of the AFF. Three locations of the canards along the ogive were considered: a forward location, such that canards could be deployed during tube launch, and two additional rearward locations that would require the canards to be deployed after launch if in a tube-launched configuration. The most rearward location was at the ogive–body interface, while the remaining location was midway between these two. The canard planform area could be increased as the location moved rearward, but the reduced moment arm resulted in little change in effective control authority. An optimization of the canard size and/or location was not deemed necessary unless the tail fin design was also allowed to change. As the comparison here was to compare two control actuation methods added to the standard AFF, the tail fin design was unchanged. As a result, the generic configuration with the canards located in the middle location, shown in Fig. 4, is representative of the performance that can be expected using typical canard control on the AFF.[5] The canard configuration variant was considered in three discrete configurations by varying the deflection angle of the canards ($\delta = 0°, 5°, 10°$). Canard deflections greater than 10° offered no significant increase in performance.

Fig. 4 Canard configuration of the AFF

3. Methodology

The initial portion of this study was completed using a commercial RANS flow solver. While the computational time for each simulation was not extreme, the combination of mesh generation and simulation time for each configuration would become too large when the larger optimization study was undertaken. As such, the feasibility of using an inviscid solver was established prior to its extensive use.

3.1 RANS Flow Solver

All of the initial configurations were simulated using CFD^{++} by Metacomp Technologies.[46] CFD^{++} was used to solve the fully 3-D RANS equation set with the realizable k-ε turbulence closure model. Several techniques such as an implicit scheme and relaxation are used to achieve faster convergence. Second-order discretization was used for the flow variables and the turbulent viscosity equation. All simulations used freestream fluid properties for air at standard, sea level,

temperature, and pressure (101325 Pa, 298 K). Supersonic Mach numbers of 2 and 3 were considered. The angle of attack, α, was varied using a quasi-steady sweep methodology, where simulations were started at the minimum α value and swept upward in 0.25° increments.[47] The angle-of-attack range investigated was limited to $-8° \leq \alpha \leq 8°$.

The computational meshes for the RANS solver were created using the unstructured mesh generator MIME by Metacomp Technologies.[46] Three views of a representative computational mesh generated by MIME are shown in Figs. 5–7. The surface mesh is created using Delaunay triangulation with the growth rate restricted to 1.2. Prism layers, with a growth rate of 1.2, are utilized to ensure boundary layer resolution. The unstructured volume mesh was allowed to grow at a rate of 1.4 to minimize the size of the overall mesh. Density boxes are implemented around the body and in the wake to control mesh growth in order to ensure adequate resolution of the shock and wake regions. The outer boundary is within 10 projectile diameters of the surface in all directions (less fore and aft) as only supersonic flow was considered. For all the configurations considered here, longitudinal symmetry is used to reduce the required computational resources. These mesh parameters had previously been found to produce reasonable results by Youn and Silton.[6] The mesh sizes were typically 9–12 million cells. Generation of the mesh was semi-automated, as the parameter file could remain the same between configurations. However, manual intervention was required for each configuration to define the geometry.

Approximately 30 min was required to generate each computational mesh. Computational resources of a Cray XC40 supercomputer (CONRAD), located at the Navy Department of Defense High Performance Computing Center, Stennis Space Center, Mississippi, were utilized for the flow solver. Each simulation (initial steady-state solution plus transient sweep) used 96 processor cores and required 6–8 h of wall clock time. All simulations were performed with the projectile in the "x"-configuration.

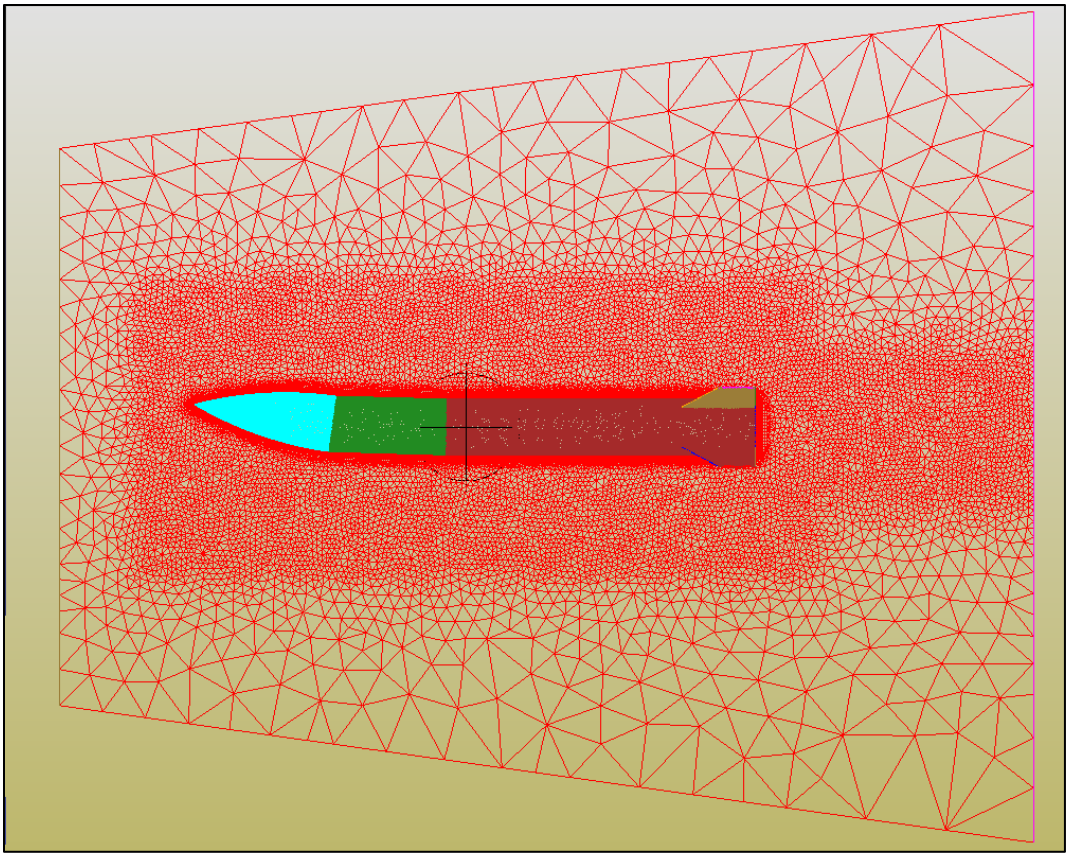

Fig. 5 Global view of an MIME-generated computational mesh

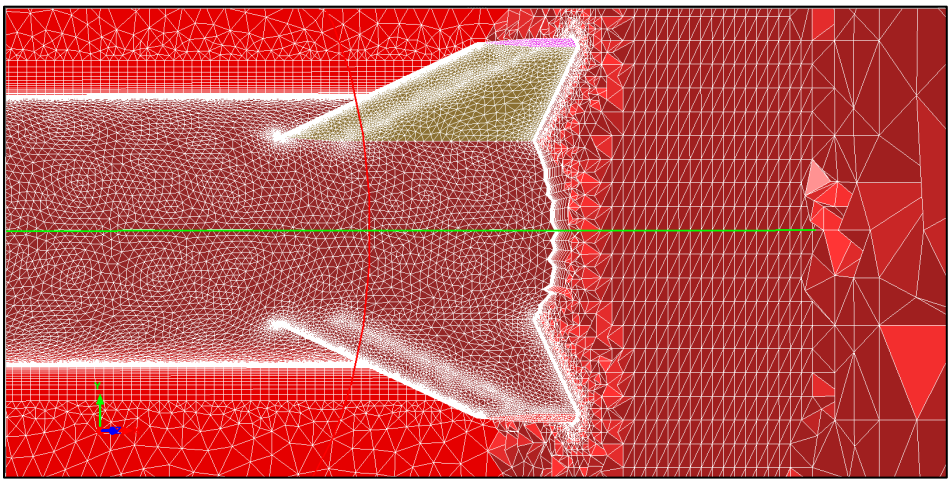

Fig. 6 Detailed perspective of aft end surface mesh and cut planes generated by MIME

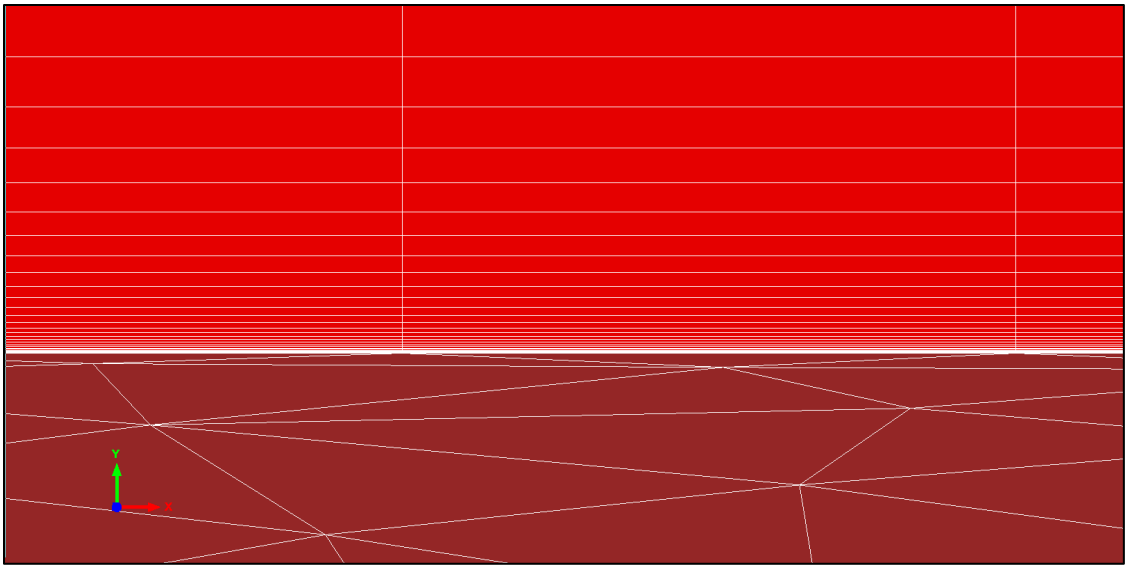

Fig. 7 Detailed perspective of boundary layer refinement generated by MIME

3.2 Inviscid Flow Solver

Cart3D is a high-fidelity inviscid analysis package for aerodynamic design. Cart3D provides utility for surface modeling and intersection, mesh generation, flow simulation, and postprocessing.[48–51] The mesh generation software with the Cart3D package produces Cartesian meshes for arbitrarily complex, watertight geometries. For the configurations considered here, a stereolithography (STL) geometry file generated using SOLIDWORKS was used to create the Cartesian mesh once the domain's extent and resolution were set.[52] The mesh generation process automatically increases the fidelity of the domain near small features and curvature present in the geometry to better resolve flow features near the surface. The option also exists to create higher-resolution areas in the wake of the body. For the Cartesian meshes generated as part of this study, the domain extended 40 projectile diameters in all directions from the center of the projectile. The resolution was chosen such that the smallest typical cell size for the domain was 0.0067 D (0.2 mm). The typical computational domain consisted of approximately 3.9 million Cartesian cells. An example of the final Cartesian mesh used is shown in Fig. 8.

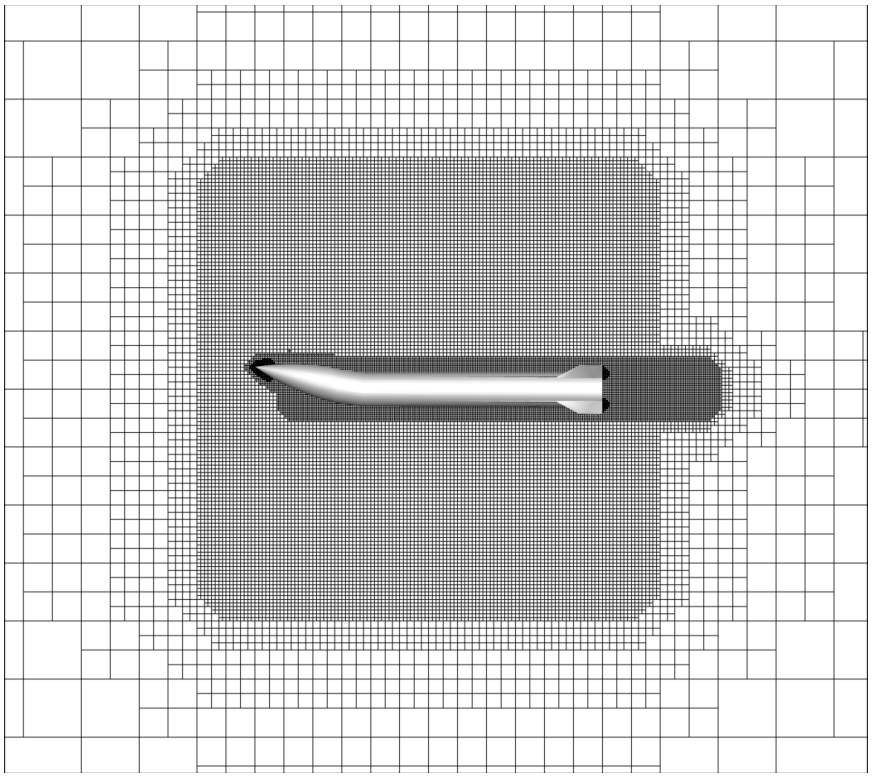

Fig. 8 Detailed perspective of a computational mesh with 40 projectile diameters (Test Case 3)

Once the mesh is generated, the flow solver, flowCart, is run using its parallelized version. The solver, which is a multilevel, linearly exact upwind solver, uses on-the-fly domain decomposition to quickly compute the aerodynamic forces and moments of a given configuration. For each configuration considered, the range of angles of attack was analyzed ($-10° \leq \alpha \leq 10°$) for the Mach number of interest. A unique steady-state simulation was completed for each α. Since the Euler equations being solved do not include the viscous components, the Cart3D analysis package provides only inviscid aerodynamic coefficients. Simulations have shown that 1) as in full Navier-Stokes simulations, it is important to ensure mesh convergence in the wake region through appropriate mesh refinement and 2) at high angles of attack the contribution of the viscous component of drag decreases as the pressure drag dominates in the body separation region leading to predictions that are closer to those in viscous solutions. The pressure component dominates in the other major static loads (C_L and C_m). Therefore, with care to take into account the limitations to predict drag, the inviscid flow solver was deemed to be an adequate tool for analyzing initial design configurations.

Mesh Resolution Study

To ensure the results of the simulations in Cart3D were mesh independent, 33 mesh parameters were adjusted and studied over 12 meshes at Mach 2 for a single bent body configuration ($\Phi_1 = 7.5°, \Phi_2 = 5.5°, Q_1 = 50.75$ m). The mesh parameters included both STL surface mesh parameters (longitudinal surface mesh discretization, surface mesh deviation, and surface mesh angle) and computational mesh parameters (computational mesh radius, computational mesh maximum refinement, density box boundaries, and density box refinement levels). The STL mesh parameter investigation was necessitated by the lack of control of surface triangle maximum aspect ratio (e.g., on cylindrical body in line with projectile axis) when output from SOLIDWORKS. Previous studies have found evidence of adverse effect on moment predictions in Cart3D.[48–51] For the current study it was determined that the STL surface mesh parameters did not significantly affect the aerodynamic coefficients. This conclusion was made by comparing the coefficient predictions from flow solutions using STL files output from SOLIDWORKS with those generated from higher-resolution STL files output from MissileLab,[53] a graphical user interface used to run several missile aerodynamic prediction codes. SOLIDWORKS' STL files were selected for ease of generation; the output parameters were modified from the default settings within SOLIDWORKS to limit the facets visible in the post-processing visualization. Some of the computational mesh parameters were found to have a significant effect on the aerodynamic coefficients, including maximum refinement, density box (defined in the following) boundaries, and density box refinement levels. Combinations of these parameters were studied over six meshes at Mach 2, $\alpha = 8°$ (detailed in Table 3). The maximum α was chosen for the investigation as the flow physics would be the most complicated and most likely to highlight shortcomings of the meshes. Table 4 shows C_D, C_L, and C_m for each test case, as well as the RANS solution. Note that C_D for the RANS solution is the total value, viscous and inviscid.

Table 3 Test case descriptions for mesh resolution study

Test case	Mesh radius	Wake density box refinement level	Body density box refinement level	Cell count
1	80 D	N/A	N/A	900,000
2	80 D	Medium	N/A	1,000,000
3	40 D	Medium	N/A	3,500,000
4	40 D	Fine	N/A	3,850,000
5	40 D	Fine	Fine	4,500,000
6	40 D	Fine	Medium	3,900,000

Table 4 Aerodynamic coefficients for mesh resolution study simulated at Mach 2, $\alpha = 8°$

Aerodynamic coefficient	Test Case 1	Test Case 2	Test Case 3	Test Case 4	Test Case 5	Test Case 6	RANS
C_D	0.6401	0.6664	0.6373	0.5972	0.6004	0.5894	0.6884
C_L	1.2612	1.2821	1.2604	1.2599	1.272	1.2581	1.3918
C_m	1.5192	1.5399	1.507	1.507	1.5562	1.5179	2.0242

A computational mesh radius of 40 projectile diameters was determined to be sufficient and effective for the computational domain. Reducing the computational mesh radius while holding all other mesh parameters constant (Cases 2 and 3) significantly increases computational mesh density without any significant change in the aerodynamic coefficients. The computational mesh density for a global mesh radius of 40 projectile diameters and a wake density box with a medium refinement in the wake is shown in Fig. 8. The wake density box was added in an attempt to increase the repeatability of the inviscid C_D prediction. The Cart3D value without the wake density box was quite similar to that obtained for the RANS simulation, not less as would be expected of an inviscid code. The addition of a mesh density box in the wake or along the body did not significantly affect C_L and C_m, as the results in Table 4 show a variation of about 1% across the six test cases. However, increasing the mesh resolution in the wake by 1) reducing the outer domain distance (80 to 40 D) and 2) using the finest wake density box resulted a decrease in C_D of 6.3% (Test Case 3 to Test Case 4 in Table 3). Figures 9 and 10 show that the wake density box provides a better-resolved wake flowfield. For the final mesh used in the study, a fine density box was chosen for the wake region. In addition, the medium refinement density box around the body was expanded to include the region on the windward side of the projectile (Test Case 6) to better refine wake features developing behind bent portions of the projectile (Fig. 11).

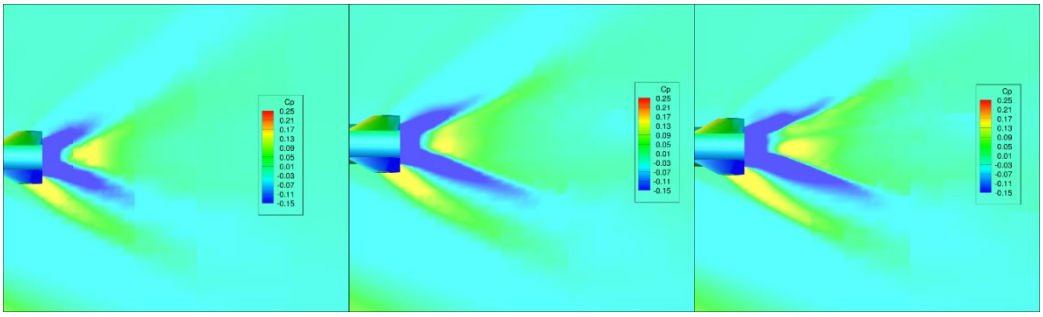

Fig. 9 C_p contours in wake of projectile for Test Case 1 (left), 2 (middle), and 3 (right)

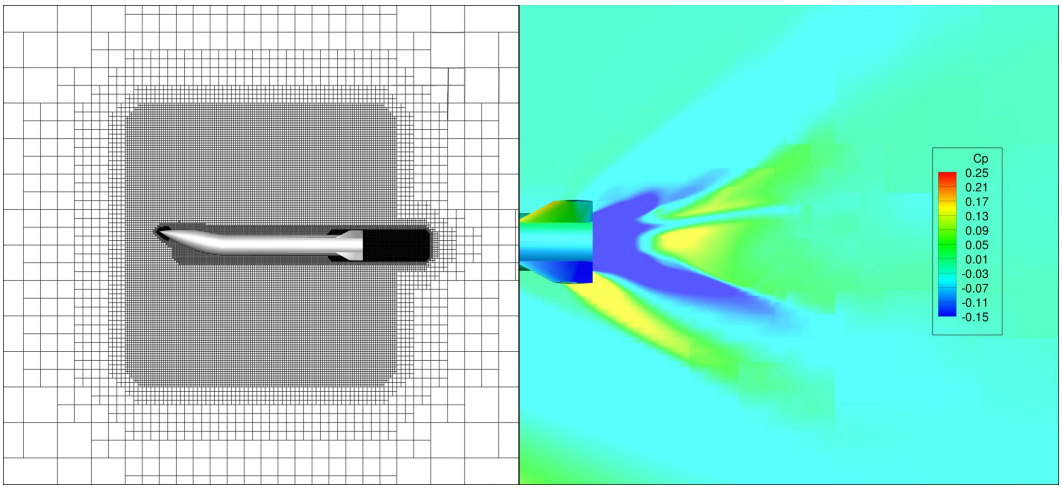

Fig. 10 Computational mesh with a heavily refined density box in the wake of the projectile (left) and resulting wake flowfield (right) for Test Case 4

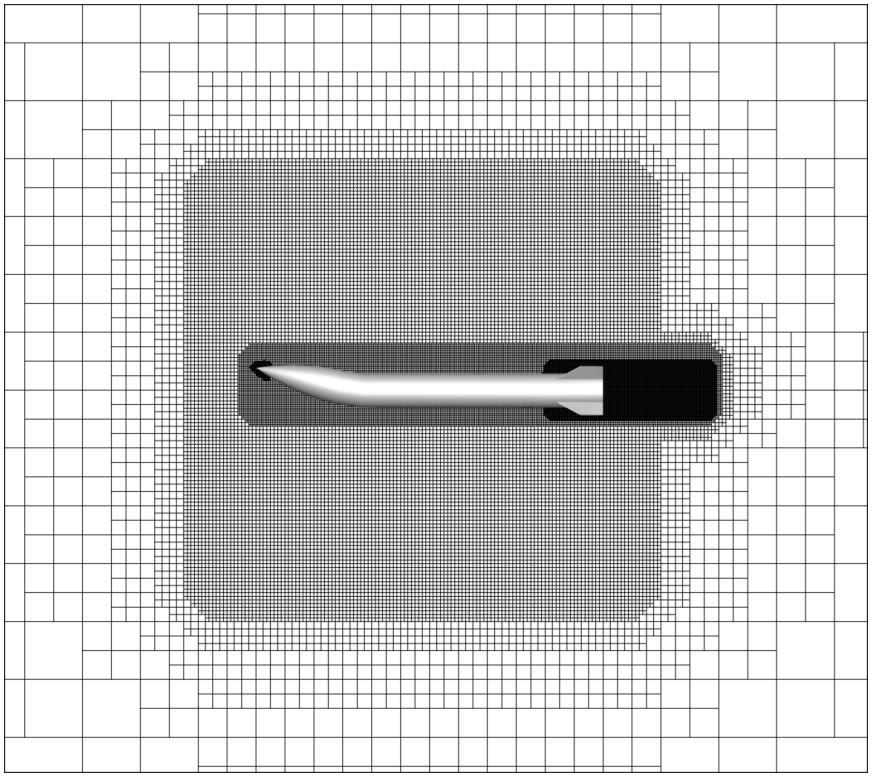

Fig. 11 Detailed perspective of a final computational mesh of a bent body projectile (Test Case 6)

3.3 Particle Swarm Optimization

Utilizing similar strategies as described in Vasile et al.,[32] PSO algorithms were used to process generations of configurations simulated by Cart3D to optimize the shape

of the bent body configuration. The essence of a PSO algorithm is that each particle in a swarm represents a design point that can move in the given design space searching for the best solution. Each particle's position is updated based on the memory of each particle as well as the knowledge gained by the swarm as a whole. Particles move through the design space according to their respective velocity (i.e., rate of change in design space parameters relative to iterations of the optimization algorithm). At each iteration, the particles are ranked in fitness according to the objective function. Once ranking is complete, the particle velocities are adjusted such that particles are oriented toward better solutions. The particle velocities then inform future particle positions in the environment. Overall, the population works together by sharing information through mathematical expressions to find progressively better solutions as the optimization routine marches through iterations. The theory is that as the number of iterations increase, the population increases in both agreement on the best solution and objective function evaluation. Once the particles in the population find enough agreement with each other or the score of the population converges by a certain statistical threshold, the optimization routine is complete. The best particle in the population at the final iteration is selected as the optimized individual. The two PSO algorithms used in this investigation were the built-in PSO algorithm in MATLAB[54] and an "in-house" PSO algorithm. The default convergence method for the MATLAB PSO algorithm focuses on the best particle in the population. Once the relative change in the best objective function value falls below the convergence criteria (i.e., $1e^{-20}$), the routine execution is considered converged. The convergence method selected for the "in-house" PSO algorithm is a variance function of the swarm's fitness.[32] The routine execution was considered converged once the variance function was evaluated below a certain tolerance (i.e., $\epsilon_{tol} = 1e^{-5}$). The equation for this convergence variance function is

$$\frac{\sum_{i=1}^{n}\left(\frac{f_i-\bar{f}}{\max([1,\max(|f_i-\bar{f}|)])}\right)^2}{n} < \epsilon_{tol} \,. \tag{1}$$

Each PSO algorithm will direct Cart3D to simulate each progressive swarm in a routine execution. Once Cart3D has completed the particle simulations, the aerodynamic data will be returned to the PSO algorithm where optimization processing will generate the identity of the next swarm. This process continues until the convergence criterion for the PSO algorithm is met. The aerodynamic data for each configuration that is simulated is saved and subsequent calls to the same configuration will access this data rather than run the simulation again. Two optimizations are considered as part of this study. The first optimization study seeks to find a bent body configuration with a maximum *L/D* at the trim condition (i.e., there is an equilibrium C_m value of zero within the α range of interest) for a given

Mach number. Maximum *L/D* was selected as an optimization goal because *L/D* is directly correlated to efficient glide flight and range metrics. For this constrained optimization problem, the evaluated bent body configurations that do not satisfy the trimmed condition are neglected. The second optimization seeks to find a bent body configuration that results to a maximum pitching moment at zero degree body angle of attack (i.e., C_{m_0}). Maximum C_{m_0} was selected as an optimization goal because C_{m_0} is directly correlated to advantages in maneuverability. In both optimizations, the aerodynamic coefficient data was fit using third-degree polynomials. Reverse linear interpolation is then used to find the root of the polynomial fit (i.e., the body trim angle). Once the trim angle is determined, linear interpolation is used to find the C_D and C_L corresponding to the trim angle. An example of the polynomial fit is shown in Fig. 12.

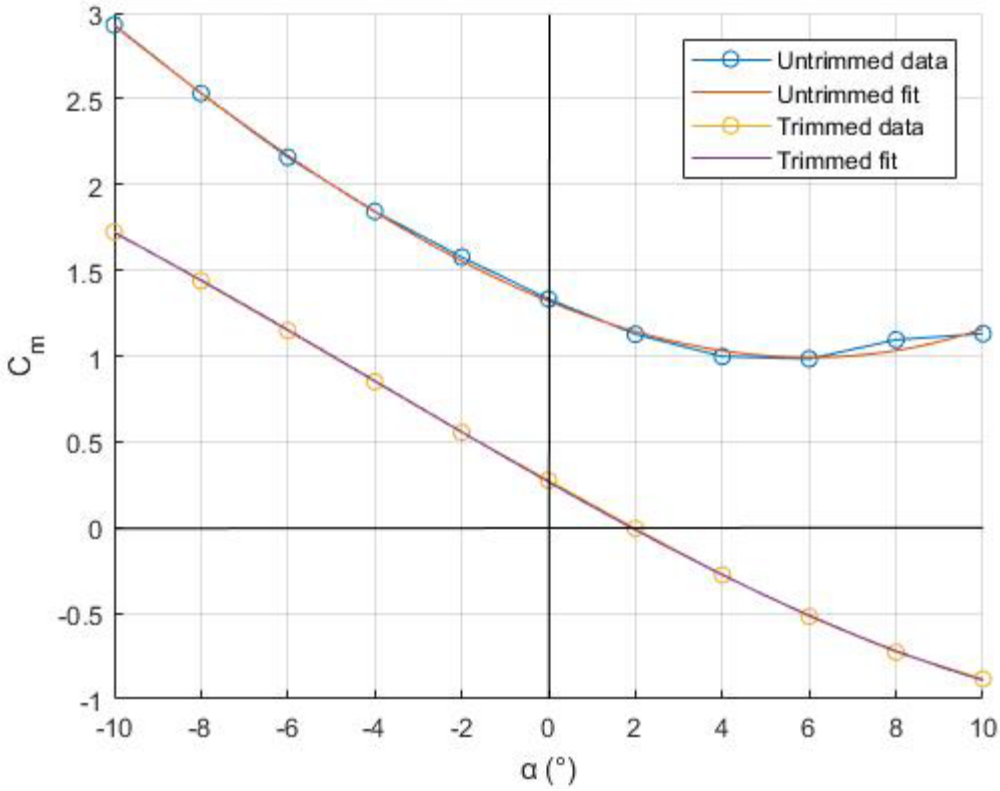

Fig. 12 Examples of C_m vs. α and the polynomial fits for one projectile that does not achieve a trimmed condition, and another projectile that achieves a trimmed condition

To assist the algorithm in converging to configurations that achieve a trimmed condition, a functional constraint is placed on configurations that do not trim. If the configuration does not trim, the minimum C_m (scaled by an amplification factor) is taken as the objective function evaluation. Configurations that result in smaller magnitudes of C_m were considered "closer to achieving a trimmed condition" and were therefore desired, and scaled accordingly. There are eight discrete options

(Table 2) for each control parameter that can characterize a given configuration. Using the three control parameters, Φ_1, Φ_2, and Q_1, the design space is represented by 512 unique configurations. The aim of these optimization studies is to find the configuration for Mach 2 that yields the most desirable results.

4. Results and Discussion

4.1 Baseline Configuration

Numerical simulations were completed for the baseline, straight body AFF (Fig. 1) at Mach 2 and Mach 3. To validate that either CFD^{++} or Cart3D could be used to obtain reasonable aerodynamic coefficients, experimental data[24–27] at Mach 2 was used for comparison. At Mach 3, numerical simulations were compared with each other, as experimental data was not available. The Mach 2 aerodynamic coefficients are presented in Figs. 13–15. By judging these data sets we can determine the efficacy of these methodologies for this particular investigation.

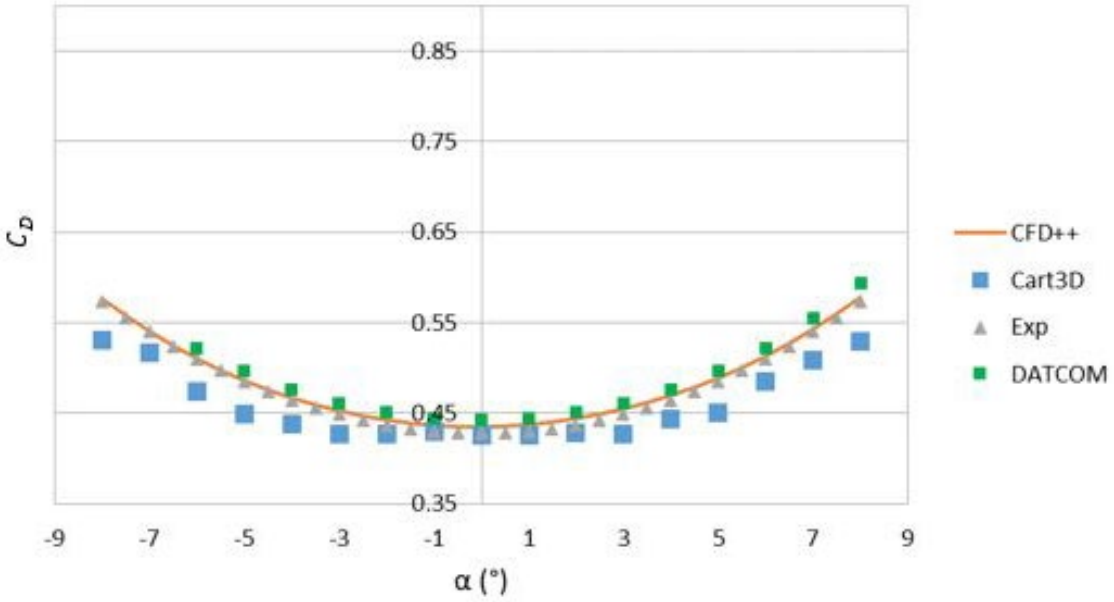

Fig. 13 C_D vs. α at Mach 2 for straight body configuration

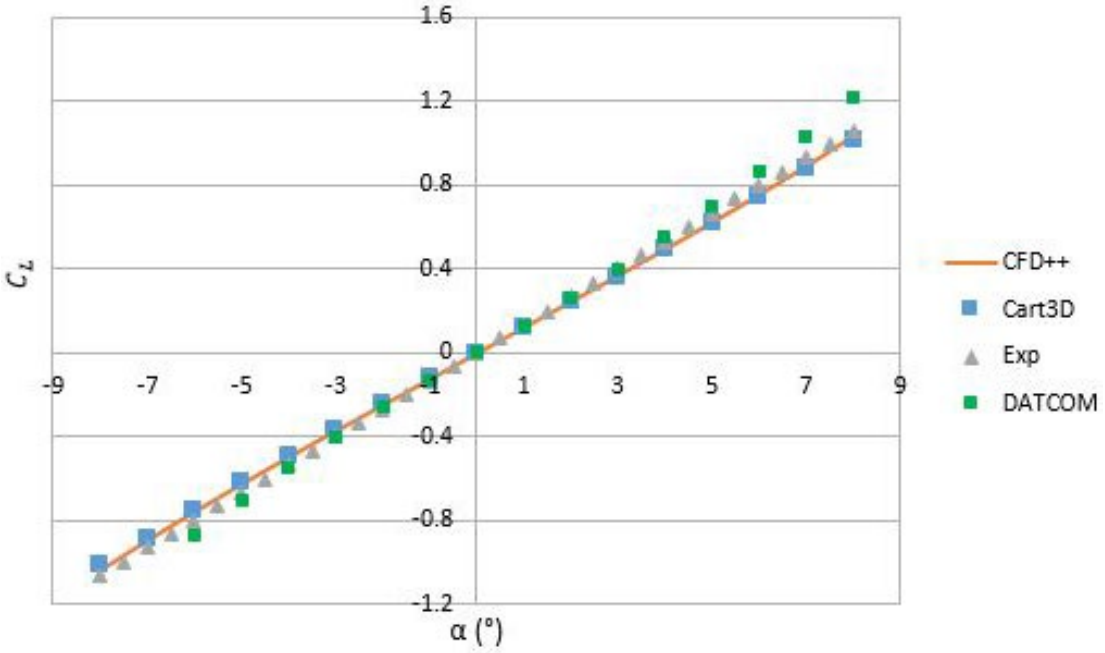

Fig. 14 C_L vs. α at Mach 2 for straight body configuration

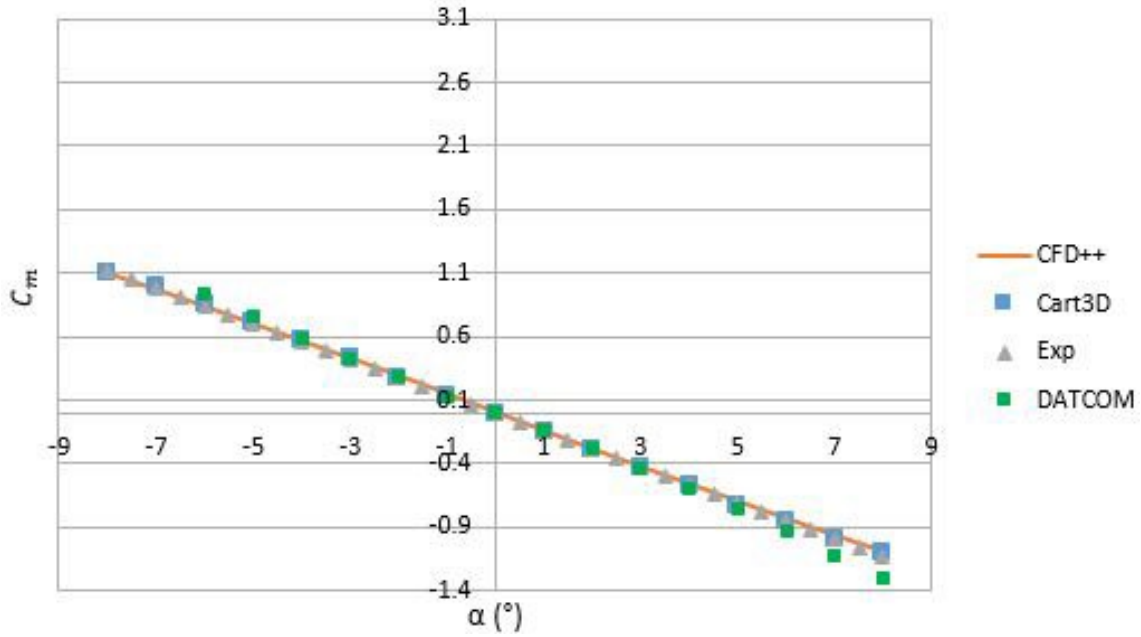

Fig. 15 C_m vs. α at Mach 2 for straight body configuration

Figure 13 shows a comparison of the drag coefficient predictions from Cart3d, CFD++, and DATCOM with experimental data. While the predictions are generally within about 10% of the experimental data, further investigation revealed that the lack of skin friction drag in the Cart3D predictions is offset by an overprediction of

the base drag by Cart3D such that the total drag coefficient is comparable among the three predictive methods. C_L and C_m are shown in Figs. 14 and 15, respectively. Agreement between the computational methodologies (viscous CFD^{++} and inviscid Cart3D) and the experimental data is good for C_L and C_m within the context of this investigation, as they primarily rely on the forebody pressure distribution. Only Missile DATCOM shows any disagreement ($|\alpha| > 5°$).

C_p contours are presented to illustrate the main flow features are present in the straight body configuration for both the Euler and RANS solutions. The C_p contours for the straight body configuration at Mach 2, α = 0° and α = 8° are shown in Figs. 16 and 17 for Cart3D and CFD^{++}, respectively. The Mach 3 C_p contours are shown in Figs. 18 and 19. Not surprisingly, there are minimal differences between the CFD^{++} and Cart3D flowfields at Mach 2 for either α. There are some minor differences in the wake flow at Mach 3 at both α, although the forebody flow is very similar even at $\alpha = 8°$.

As expected, the α = 0° cases at Mach 2 and 3 (Figs. 16 and 18) are symmetric. Additionally, the shock is stronger for the Mach 3 case. At α = 8°, at both Mach 2 (Fig. 17) and Mach 3 (Fig. 19), the shock on the windward side of the nosecone significantly stronger than the shock on the leeward side of the nosecone due to the asymmetric nature of the flow. The curvature of the shock due to the ogive nose cone is present at both Mach numbers, but more evident with the stronger Mach 3 shock. The flow behind the bow shock is relatively uniform until it passes over the four fins where shock interactions occur.

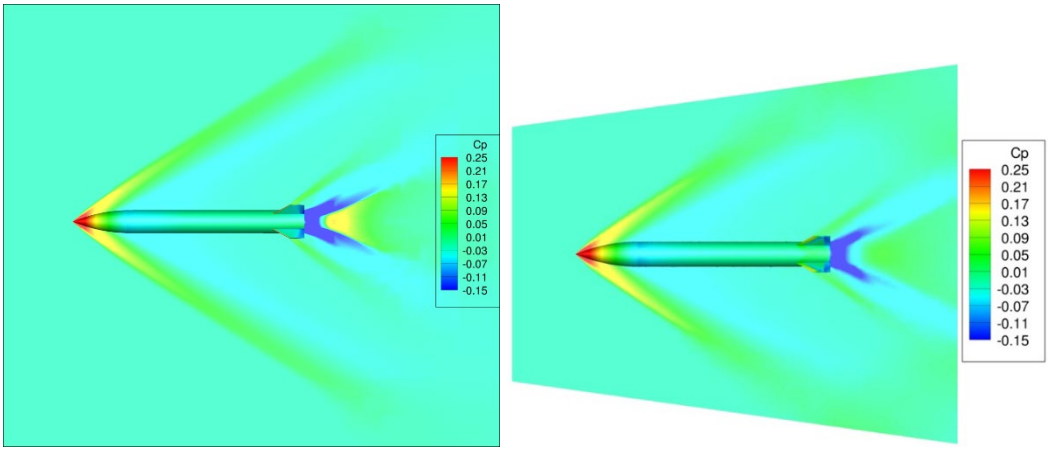

Fig. 16 C_p contours at Mach 2: $\alpha = 0°$ from Cart3D (left) and CFD^{++} (right)

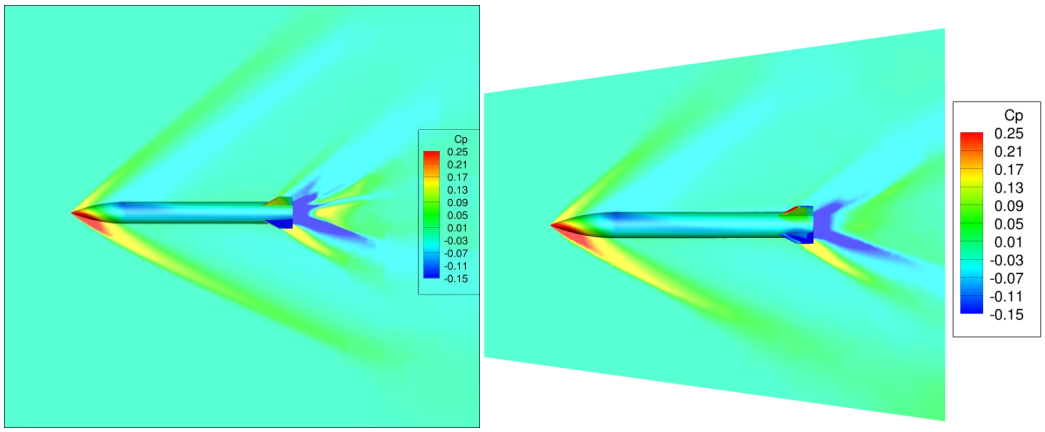

Fig. 17 C_p **contours at Mach 2,** $\alpha = 8°$ **from Cart3D (left) and CFD^{++} (right)**

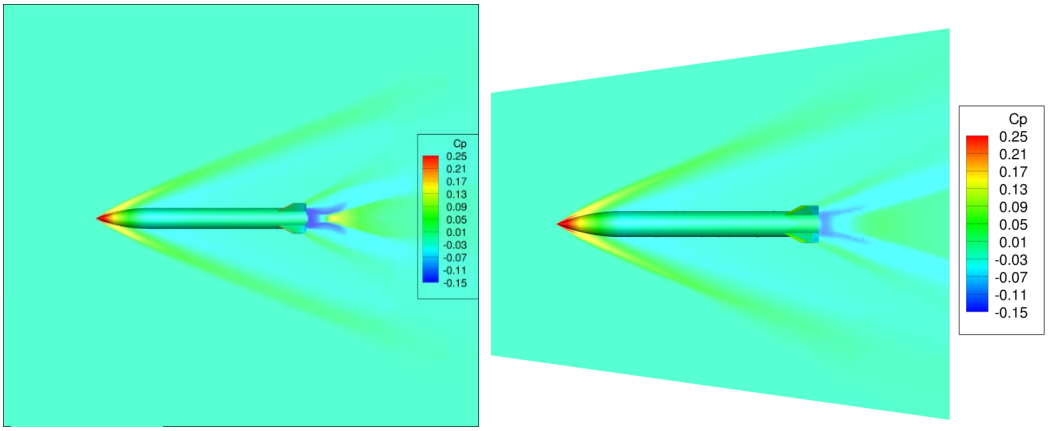

Fig. 18 C_p **contours at Mach 3,** $\alpha = 0°$ **from Cart3D (left) and CFD^{++} (right)**

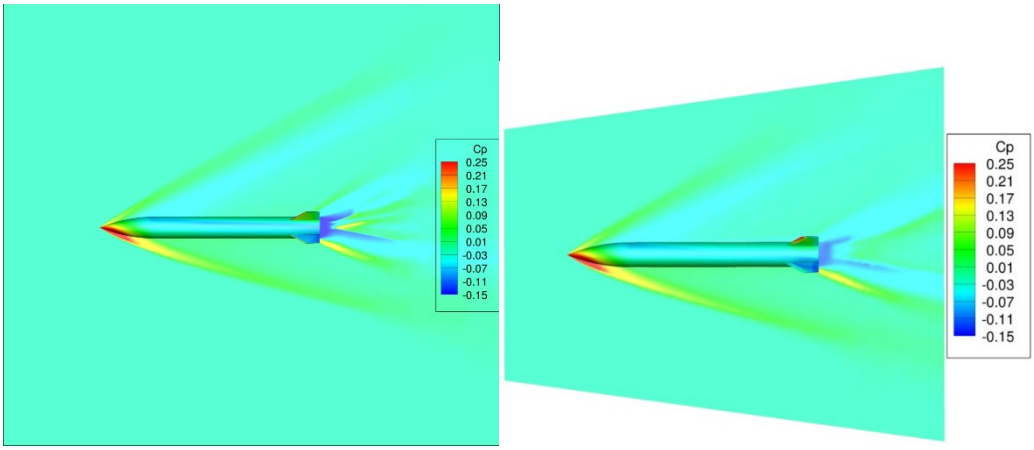

Fig. 19 C_p **contours at Mach 3,** $\alpha = 8°$ **from Cart3D (left) and CFD^{++} (right)**

4.2 Initial Bent Body Configurations

A random population of bent body configurations (bending in only one direction) was simulated in CFD^{++}, and the aerodynamic coefficients were obtained to gain a general perspective on the aerodynamic characterization of this design concept. The plots for C_D, C_L, and C_m of the random population are shown for Mach 2 and Mach 3 in Figs. 20–22 and Figs. 23–25, respectively. A subset of configurations (from Table 2, shown as thicker lines in Figures 20–25) was selected for in-depth study based on C_m at Mach 2 (Fig. 26). These bent body models were selected as representative of all configurations. Model 5 has small bend angles and trims (α at which projectile is in static equilibrium, i.e., $C_m = 0$) at relatively small α; Model 2 appears to just reach a trimmed condition at $\alpha = 7°$. Neither Model 3 nor Model 4 reaches a trimmed condition in the range of α investigated, but Model 3 appears to be less unstable that Model 4. For a bent body maneuver, projectile static stability is not considered a requirement at this time. Further analyses of actuator and vehicle response times are still needed to determine if vehicle control can be maintained upon returning to the straight body configuration. At Mach 3, only Model 5 reaches a trimmed condition in this range of α (Fig. 25). In Figs. 20–25, the legend only includes, for simplicity, the particular configurations under investigation, which are also bold.

Figure 20 (Mach 2) and Fig. 23 (Mach 3) both show asymmetry in C_D. The variation in C_D is significantly less at negative α than at positive α. The magnitude of C_D is smaller at negative α than at the same positive α for all configurations other than the straight body configuration. This is to be expected, as bending in the same direction as α results in a greater projected area to the freestream velocity than bending opposite to the freestream velocity. This also leads to asymmetric behavior in C_L, and C_m.

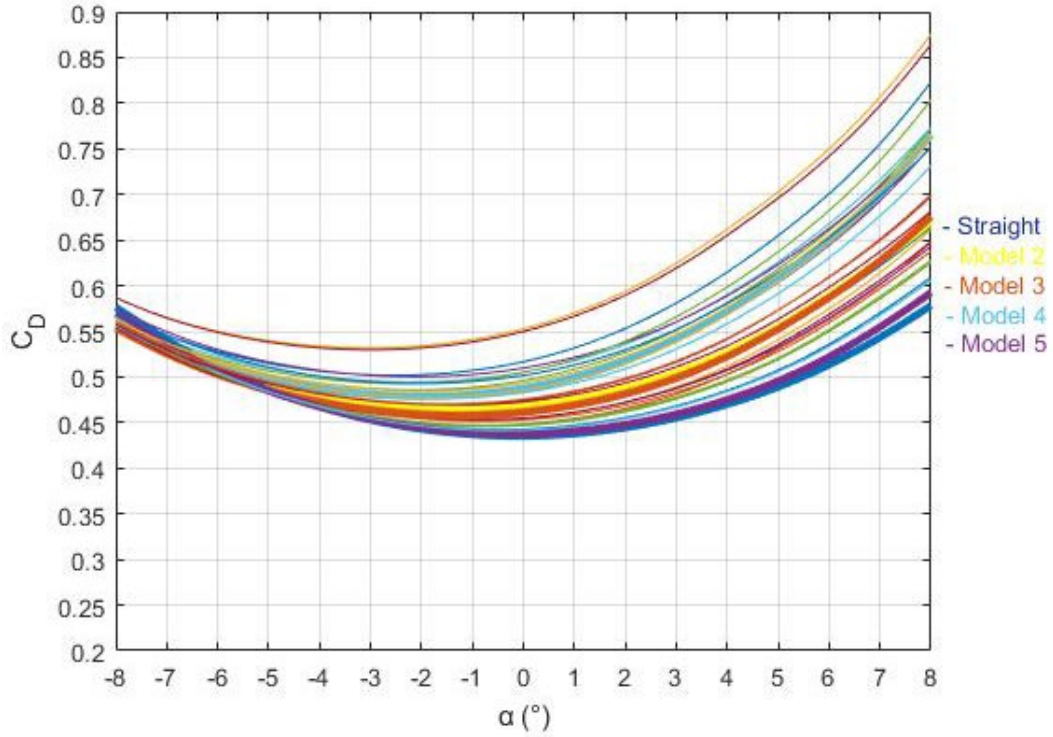

Fig. 20 C_D vs. α at Mach 2 for population of bent body models

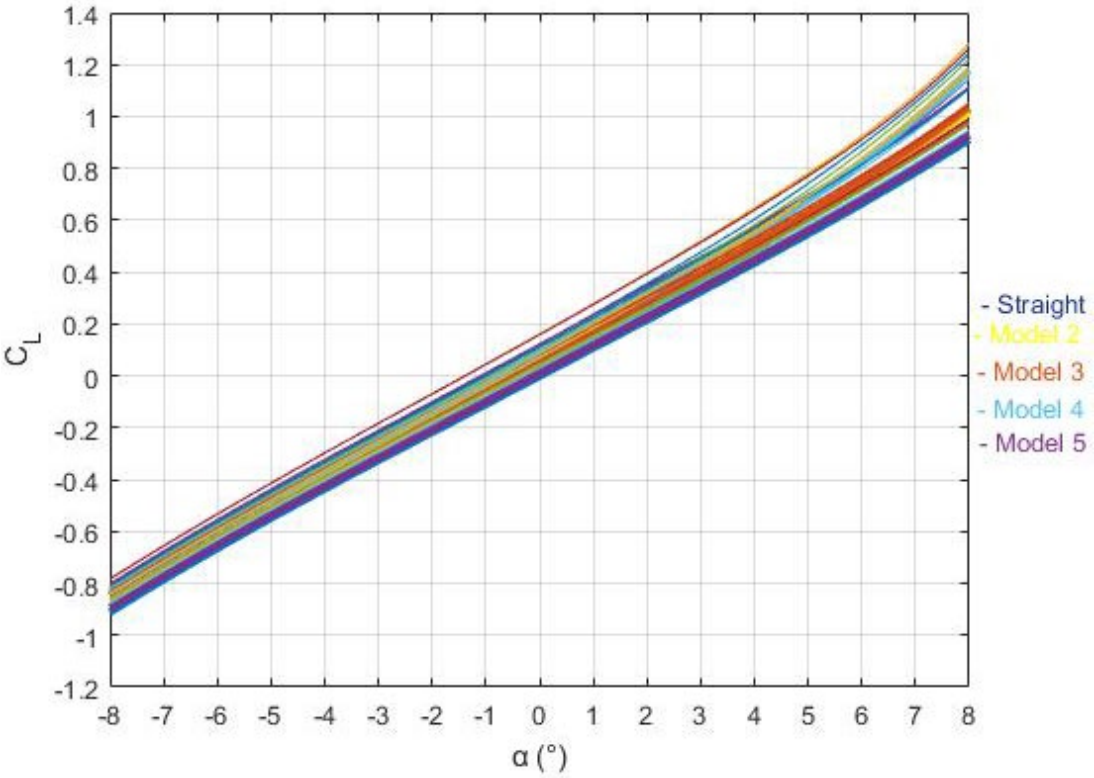

Fig. 21 C_L vs. α at Mach 2 for population of bent body models

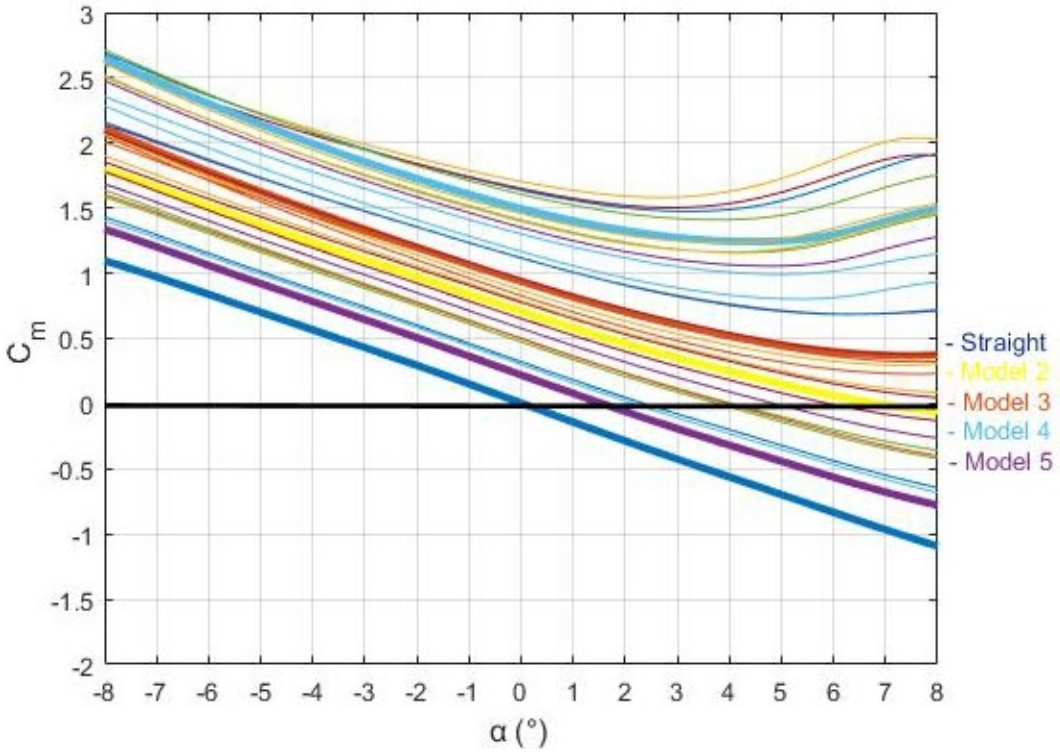

Fig. 22 C_m vs. α at Mach 2 for population of bent body models

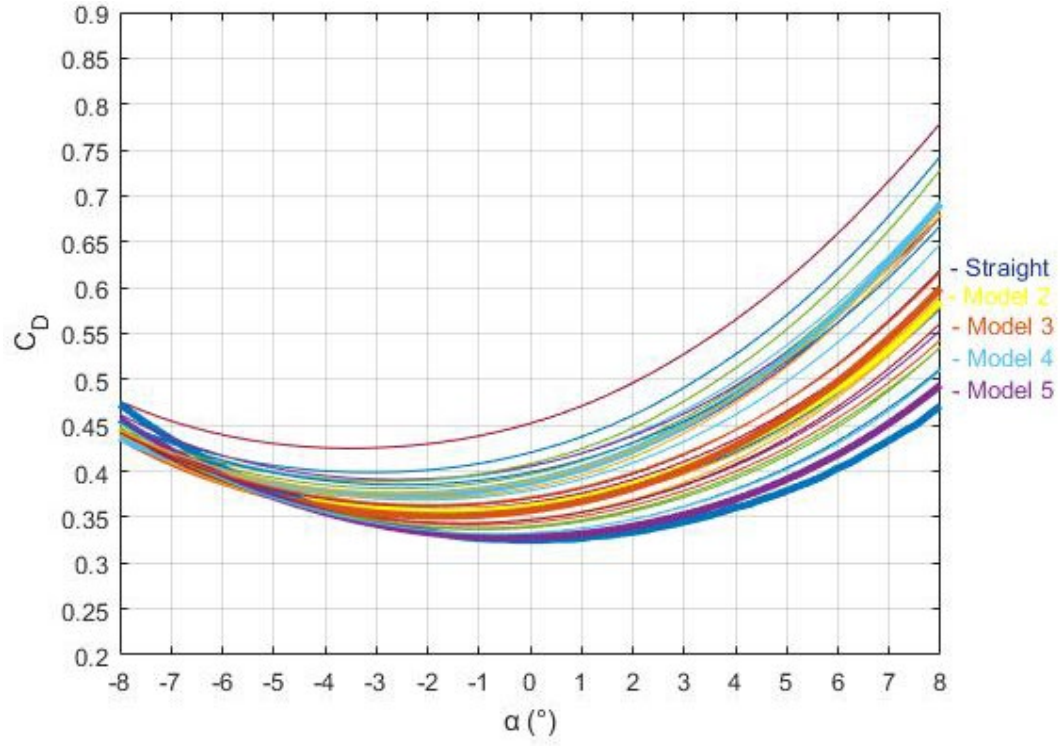

Fig. 23 C_D vs. α at Mach 3 for population of bent body models

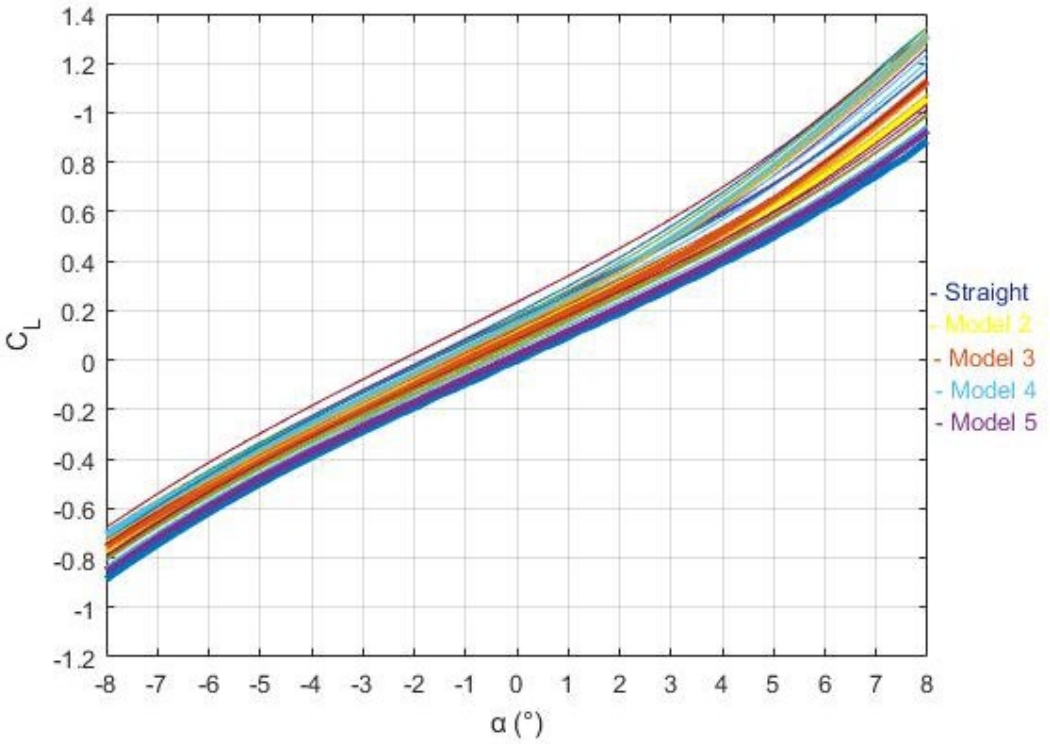

Fig. 24 C_L vs. α at Mach 3 for population of bent body models

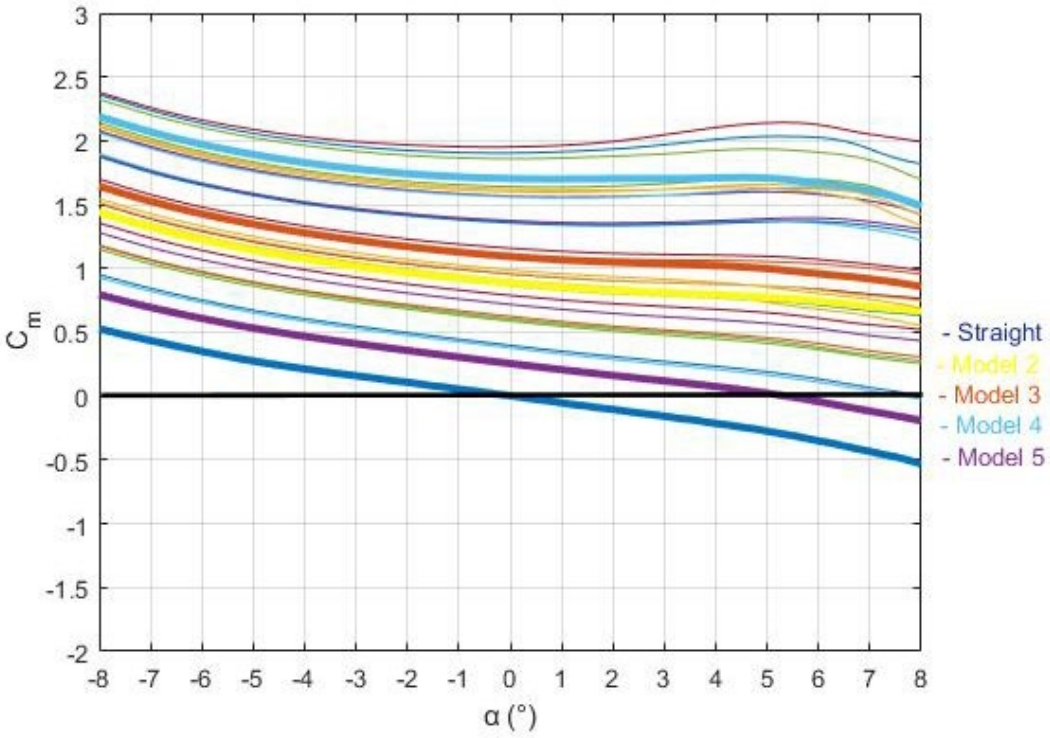

Fig. 25 C_m vs. α at Mach 3 for population of bent body models

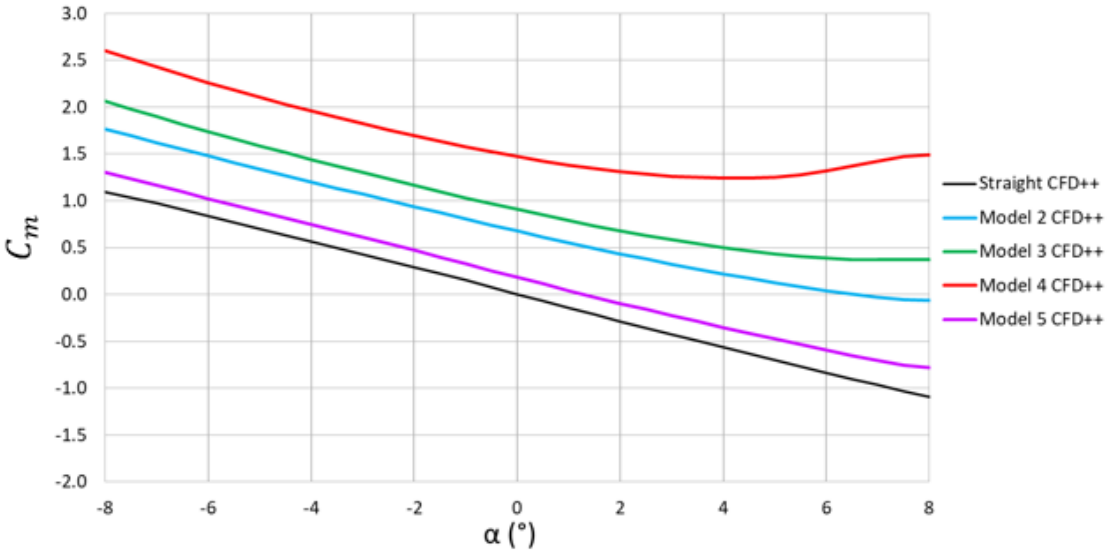

Fig. 26 C_m vs. α at Mach 2 for chosen subset of bent body models

C_L is plotted in Fig. 21 and Fig. 24 for Mach 2 and Mach 3, respectively. There is significantly less variation with configuration than was seen in C_D, but there is an increase in magnitude difference of C_L among the configurations as α increases (i.e., the spread of values is greater). This again follows from the fact that the asymmetric, bent configurations, as configured here, will provide a greater effective angle of attack at positive angles of attack.

Figures 22 and 25 show both expected and unique features for C_m. As expected, the slope of C_m at Mach 3 is shallower than at Mach 2. For the straight body configuration, this indicates that AFF at Mach 2 is more statically stable than at Mach 3, which is typical of a supersonic projectile. Decreased stability at Mach 3 also affects the bent body configurations; 10 of the bent body configurations investigated reach a trimmed condition at Mach 2, while only 1 does so at Mach 3. Also at Mach 2, C_m of the straight body configuration as well as the less bent configurations varies approximately linearly with α, while at Mach 3 it is a cubic dependency. For these configurations, the bent body configurations appear to be no more than a shift in C_m value at $\alpha = 0°$ (Model 5). As Φ_1 and Φ_2 continue to increase, slope of C_m begins to decrease with increasing α (Model 2). In fact, for some of the configurations with the largest Φ_1 and Φ_2, C_m reaches a minimum and begins to increase (Model 3); in the most extreme cases, a local maximum is reached as well (Model 4). This local maximum may be due to a stall effect of the flow over the bent section. The result is divergence and a significant range of C_m across the configurations.

The initial CFD^{++} simulations demonstrated that significant computational resources and arduous/nonautomated meshing would be required to obtain an

optimized configuration for the bent body, which would not be feasible. As such, a more efficient (i.e., automated) method was sought. The aeroprediction code Missile DATCOM has a documented method of implementing the bent body configuration by assigning a "camber" to the centerline axis.[38] However, there are limited validation cases available in Missile DATCOM, and the authors felt an "intermediate-level" code, such as Cart3D, would provide the necessary throughput, while providing information on the flowfield that would be valuable in understanding and evaluating the relative performance of the bent configurations. While reasonable results were obtained for the baseline AFF configuration, evaluation of Cart3D for the bent body configurations is necessary prior to full implementation. The four models referenced (Table 2) were chosen to highlight possible differences. The aerodynamic coefficients for these four bent body models were compared between the two flow solvers, Cart3D to CFD^{++}. C_D, C_L, C_L/C_D, and C_m are compared at Mach 3 (Figs. 27–30, respectively). C_D is shown in Fig. 27 for Cart3D (only inviscid available), CFD^{++} (total, viscous, and inviscid), and the CFD^{++} inviscid-only component (labeled CFD^{++} inv) for each bent body model. Figures 28–30 include only the Cart3D and total CFD^{++} results, as the viscous component of C_L and C_m is generally small.

Cart3D predicts forebody pressure drag well compared to DATCOM and RANS CFD but tends to overpredict base drag. The difference in base drag is not unexpected since the viscous wake in the base region that contributes to the base drag is not physically modeled using the inviscid Cart3D technique. The overprediction of base drag in Cart3D is offset by the lack of skin-friction drag in the total drag prediction such that the total drag predicted is comparable to DATCOM and RANS CFD predictions. Predominant variations calculating drag in Cart3D are due to changes in forebody pressure drag, which is largely an inviscid phenomenon well predicted by Cart3D.

The primary investigation of this report seeks to optimize the pitching moment at zero degrees angle of attack and maximum lift-to-drag ratio at the trim angle of attack. The pitching moment at zero degrees angle of attack should be well predicted by the forebody component of pitching moment. For lift-to-drag ratio at the trim condition, both the trim angle of attack and lift at the trim angle of attack should be reasonably well predicted due to accurately calculating the forebody component of normal/lift force and pitching moment in Cart3D. Although there are inaccuracies calculating the drag contribution to lift-to-drag ratio, Cart3D still produces reasonable predictions of total drag while also including the relevant effects of variation in drag due to angle of attack and nose bentness.

The Cart3D predicted C_D is a little higher than expected compared to the inviscid component of the CFD^{++} prediction for the straight body configuration (Fig. 27).

However, Cart3D predicted C_D for the bent body configurations correlate better with total C_D calculated by CFD^{++}. This is possibly because in the bent body configurations a larger component of the drag is due to pressure drag behind the bent section. As a lower percentage of the drag is due to viscous effects, the inviscid calculation is able to predict a higher percentage of the total drag. The *L/D* values calculated using Cart3D predictions should therefore also be reasonable for this study.

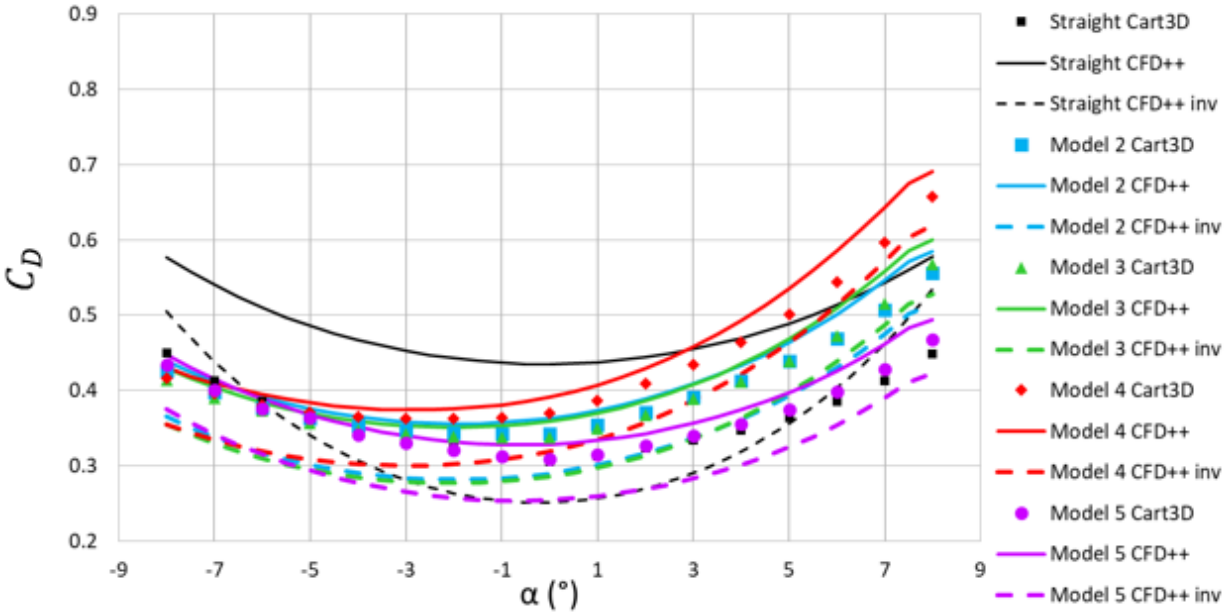

Fig. 27 C_D vs. α at Mach 3 for select bent body models

Figure 28 shows there is generally little difference between the flow solver results for C_L, although the differences increase as α increases. Although small, the Cart3D result for each model is less than the CFD^{++} result at every angle of attack. This is an expected result because in Cart3D, vortices will roll up at larger α, because it has to rely on the curvature of the body alone, and not the rotation induced by the viscous boundary layer. Besides this difference, there is still generally good agreement between Cart3D and CFD^{++}. Comparing the *L/D* between Cart3D and CFD^{++} (Fig. 29), there is good agreement between the flow solvers for the bent body configurations investigated here, indicating Cart3D is likely adequate for our analysis.

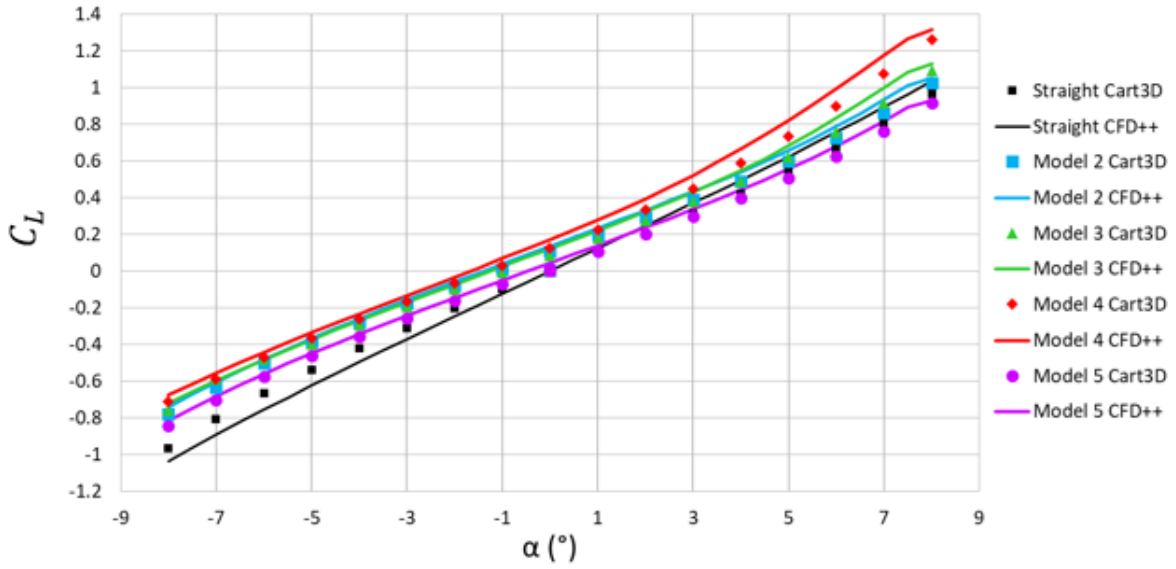

Fig. 28 C_L vs. α at Mach 3 for bent body models

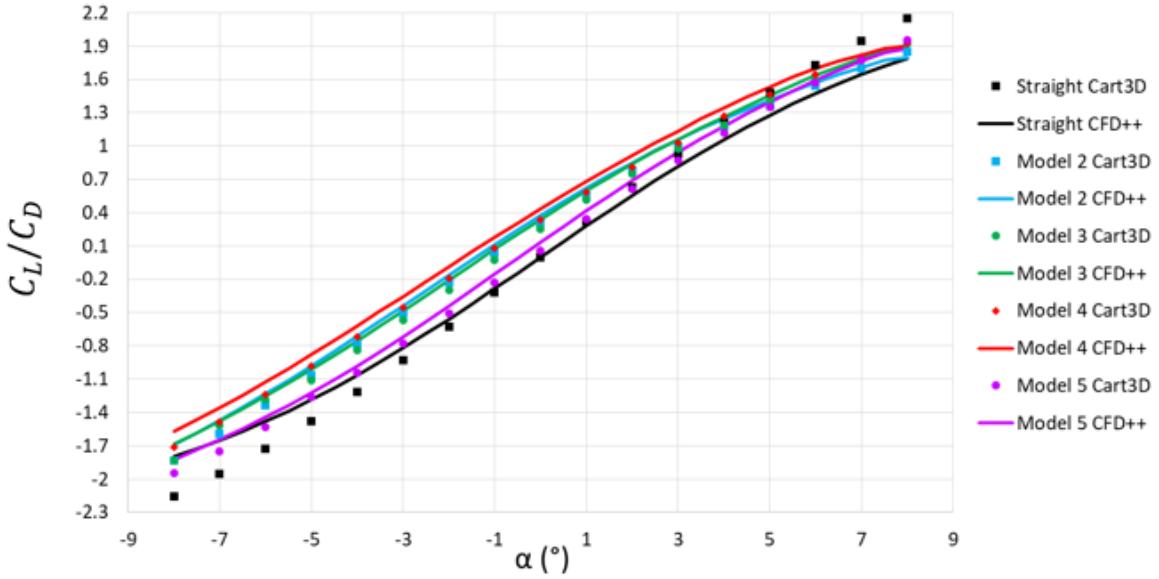

Fig. 29 *L/D* vs. α at Mach 3 for select bent body models

Figure 30 shows very good agreement between Cart3D and CFD^{++} for C_m on each model. From this plot, we see that only Model 5 can trim at Mach 3: predicted at $\alpha = 5°$ for CFD^{++} and $\alpha = 7°$ Cart3D. The rest of the models are unstable at all $\alpha < 8°$. Again, a statically unstable configuration is not a concern as the control algorithm would be expected to have the projectile fly in the baseline, straight body configuration for most of the flight, morphing to the unstable, bent body configuration when maneuver was desired.

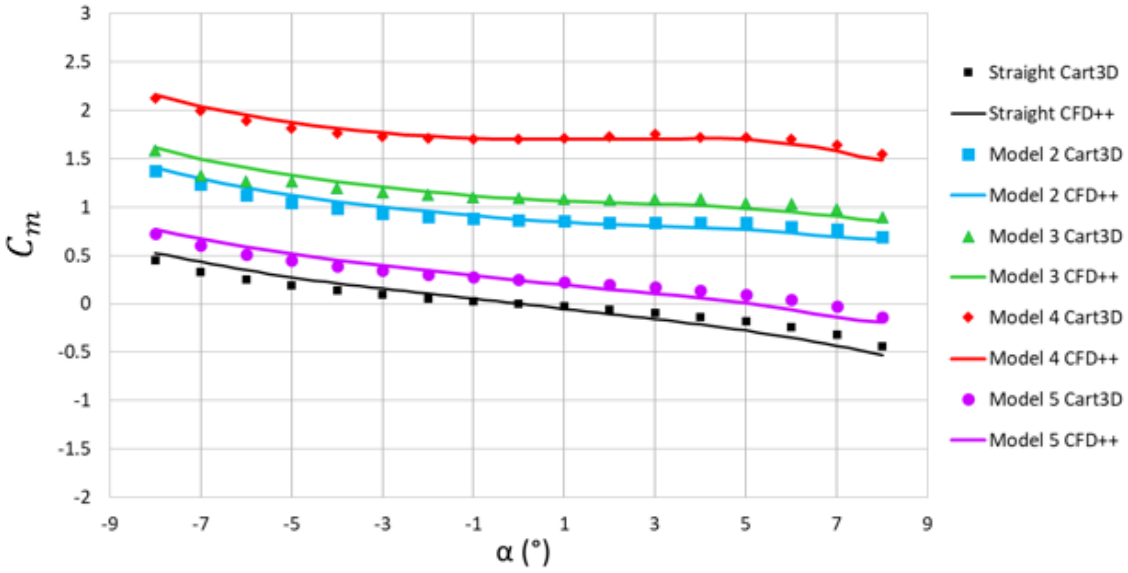

Fig. 30 C_m vs. α at Mach 3 for bent body models

Pressure coefficient contours are presented for each of the bent body models for Mach 3 at $\alpha = 0°$ and $\alpha = 8°$ in Figs. 31–38. In each figure, the Cart3D solution is on the left and the CFD^{++} solution is on the right. Comparing the Cart3D and CFD^{++} flow field solutions reveal that the only significant differences are in the wake for any of these configurations. Thus, future studies could be conducted with reasonable reliability using Cart3D rather than CFD^{++} to minimize resource use. Additionally, mesh refinement, with concentration on the wake region, should be completed to ensure proper resolution for both solvers. At present, no analysis of the vortices being shed from the forebody has been conducted, which could also account for differences observed in the coefficients.

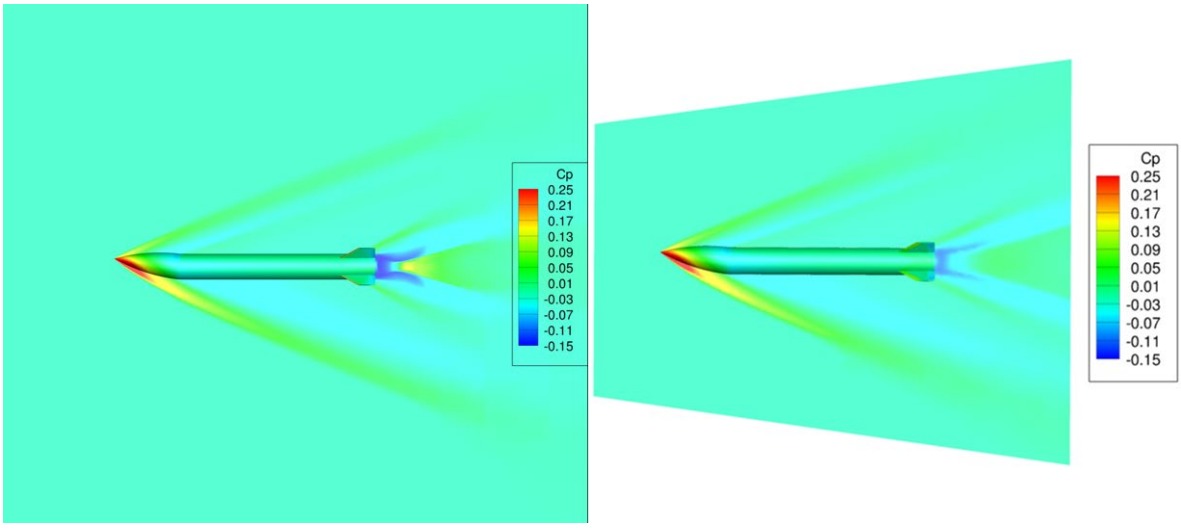

Fig. 31 C_p contours at Mach 3: $\alpha = 0°$ from Cart3D (left) and CFD^{++} (right) for Model 2

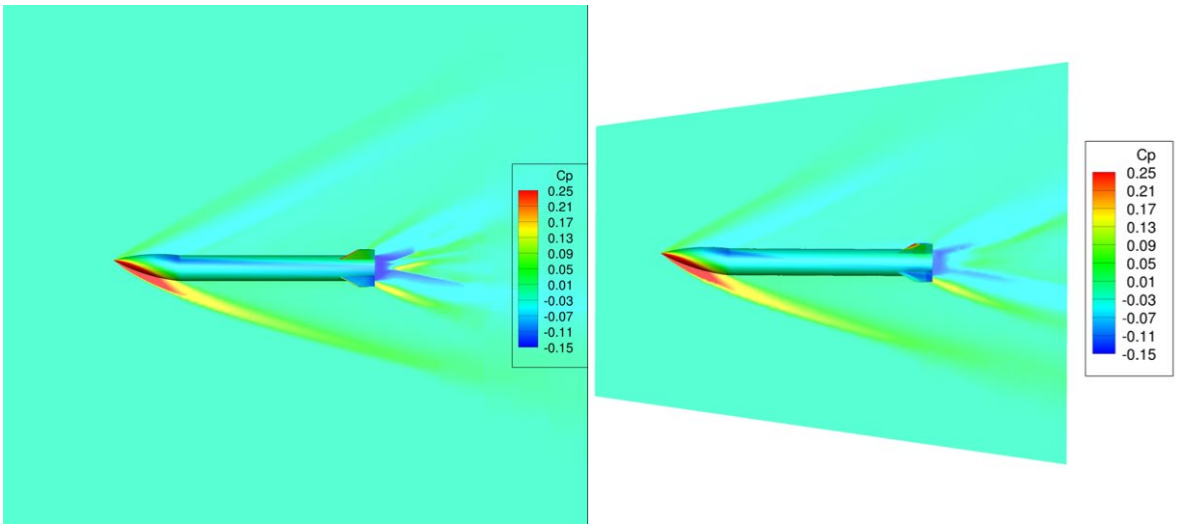

Fig. 32 C_p **contours at Mach 3:** $\alpha = 8°$ **from Cart3D (left) and CFD^{++} (right) for Model 2**

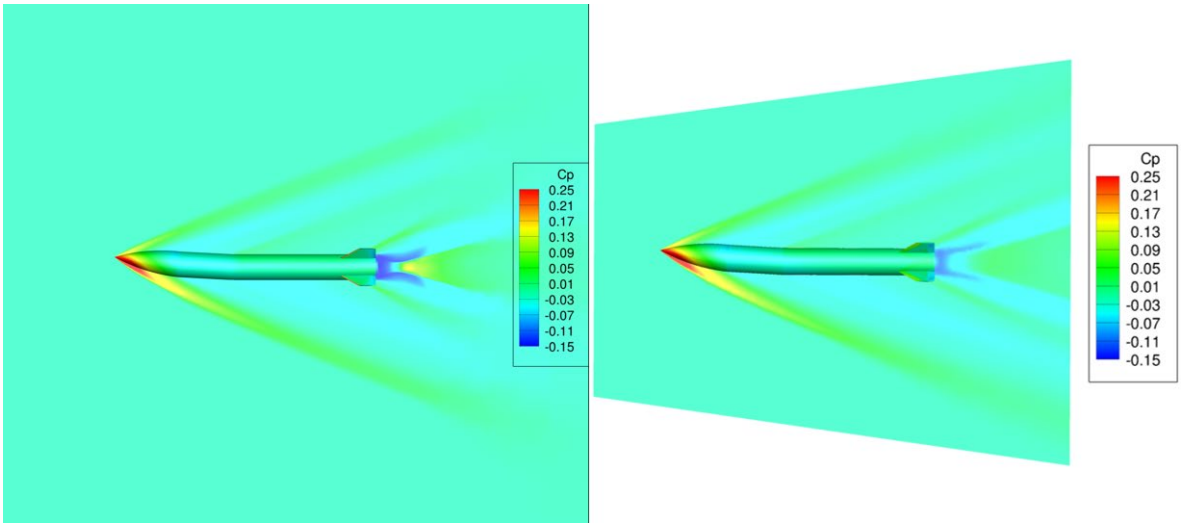

Fig. 33 C_p **contours at Mach 3:** $\alpha = 0°$ **from Cart3D (left) and CFD^{++} (right) for Model 3**

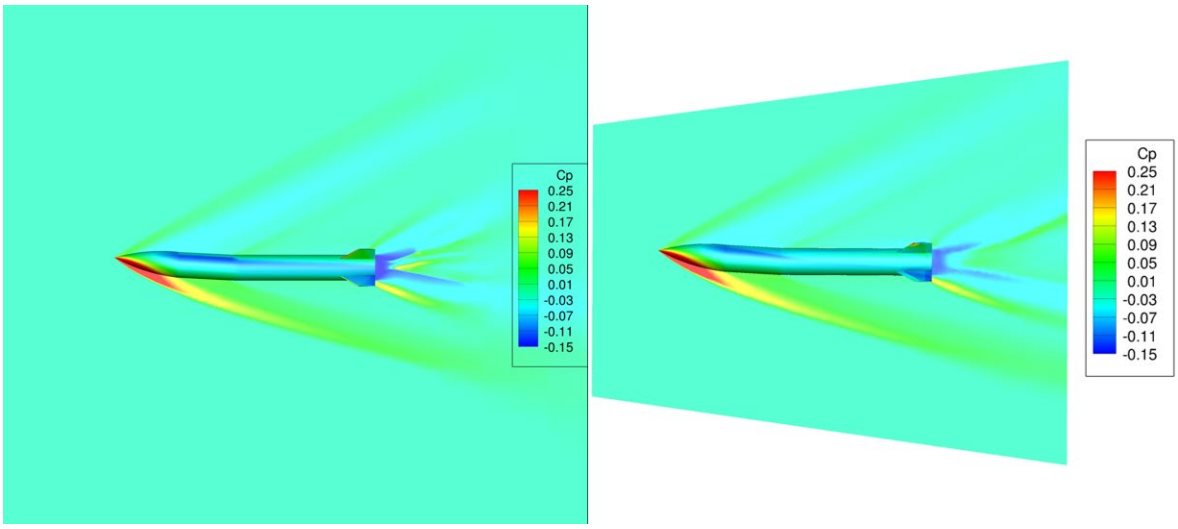

Fig. 34 C_p **contours at Mach 3:** $\alpha = 8°$ **from Cart3D (left) and CFD^{++} (right) for Model 3**

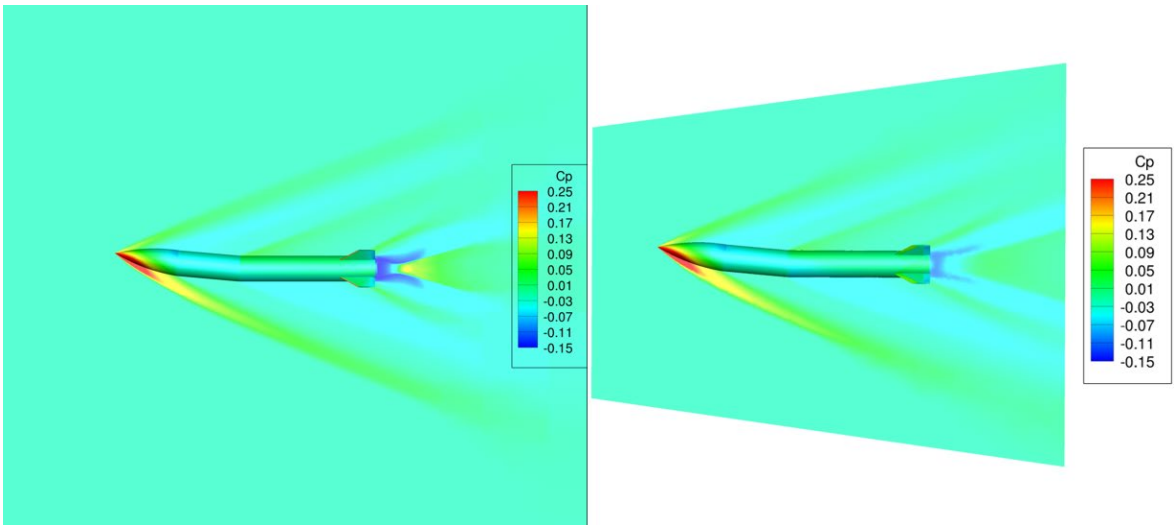

Fig. 35 C_p **contours at Mach 3:** $\alpha = 0°$ **from Cart3D (left) and CFD^{++} (right) for Model 4**

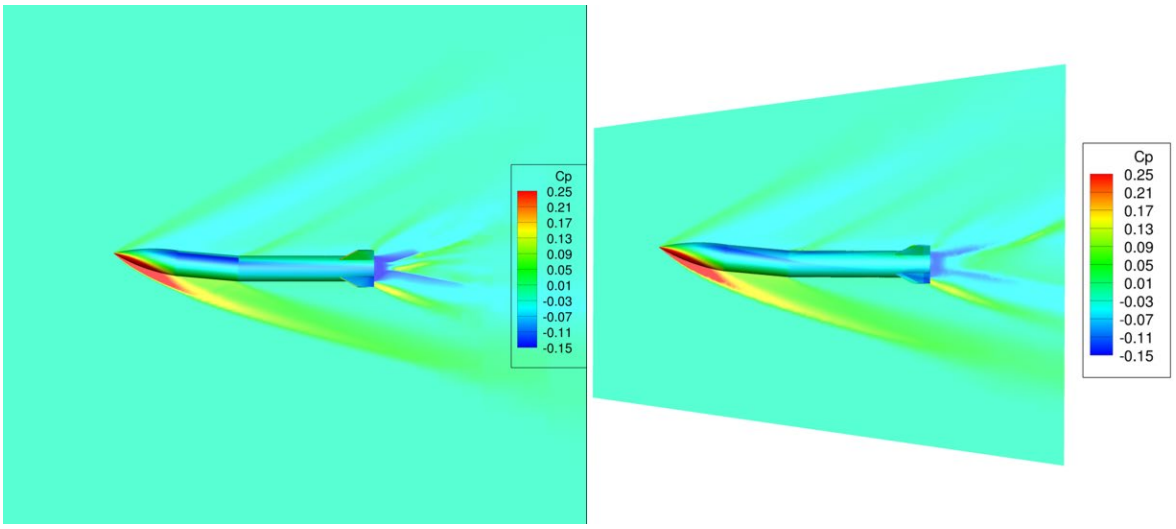

Fig. 36 C_p **contours at Mach 3:** $\alpha = 8°$ **from Cart3D (left) and CFD^{++} (right) for Model 4**

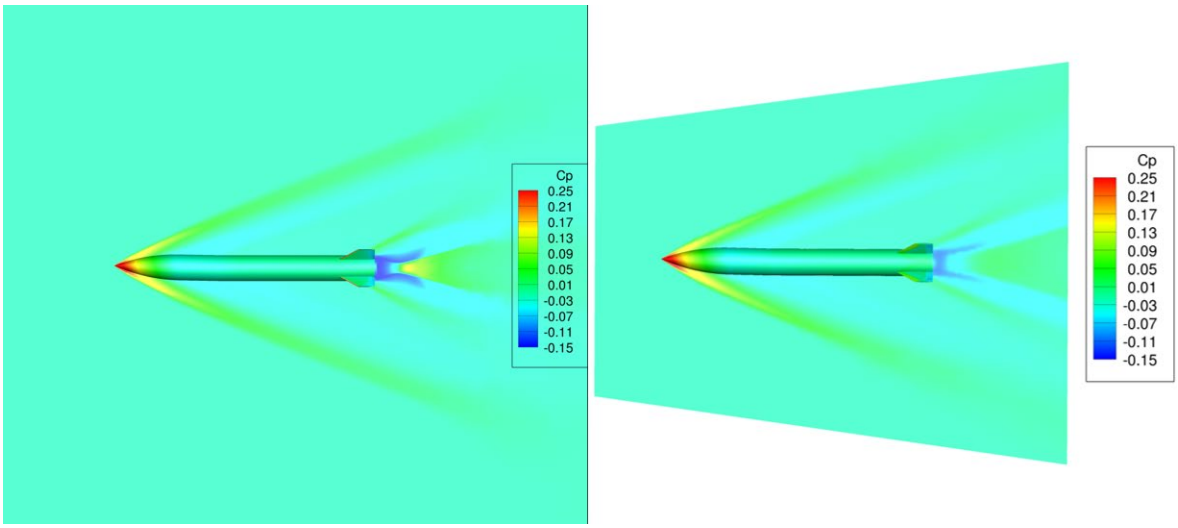

Fig. 37 C_p **contours at Mach 3:** $\alpha = 0°$ **from Cart3D (left) and CFD^{++} (right) for Model 5**

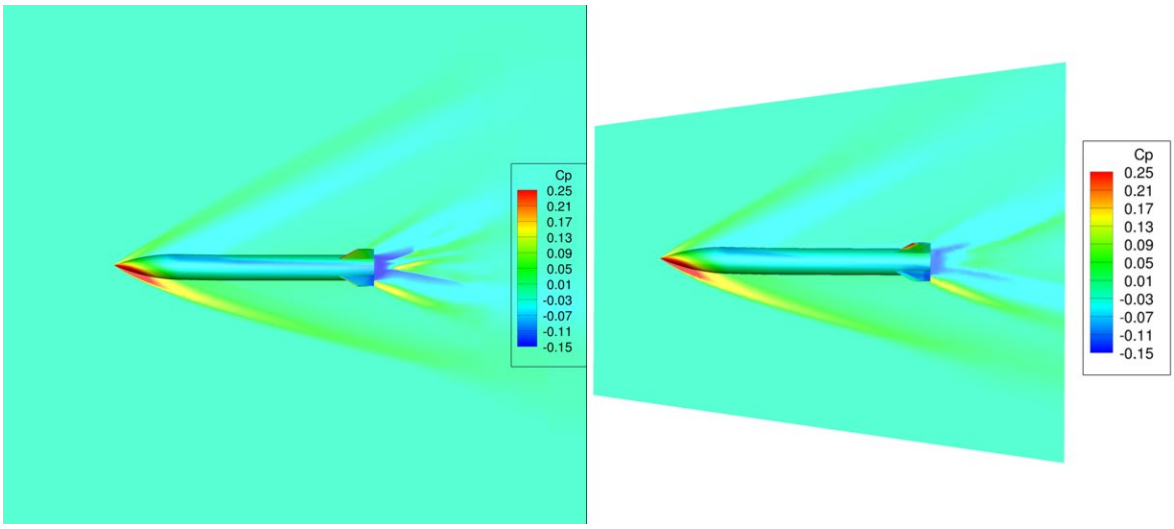

Fig. 38 C_p contours at Mach 3: $\alpha = 8°$ from Cart3D (left) and CFD^{++} (right) for Model 5

4.3 Design Space Analysis

The availability of high-performance computers and the resulting speed of Cart3D in providing solutions allowed solutions to be computed for the entire design space (512 unique configurations) of the problem prior to running optimization routines. The design space in this case is the combinatorial summation of all three parameters from Table 2. Although typically not possible to compute a priori all the possible configurations to be used in the optimization process, in this case it allowed us to investigate multiple optimization methodologies. Assessing the plots of all of the data can help us attain a broad perspective of the problem to be optimized. Figure 39 displays the aerodynamic coefficients versus α for C_m, C_L, and C_D for the entire set of 512 unique configurations at Mach 2 and the range of α investigated ($-10° \leq \alpha \leq 10°$). As expected, the general shape of these plots match those observed in the previous section, which highlighted 31 of the 512 configurations shown. As predicted, the trends in aerodynamic coefficients versus α were essentially the same for the 512 configurations as they were for the first random set of 31 configurations. The magnitude of the "bentness" of the projectile has little effect at large negative α as the total "effective" α is reduced.

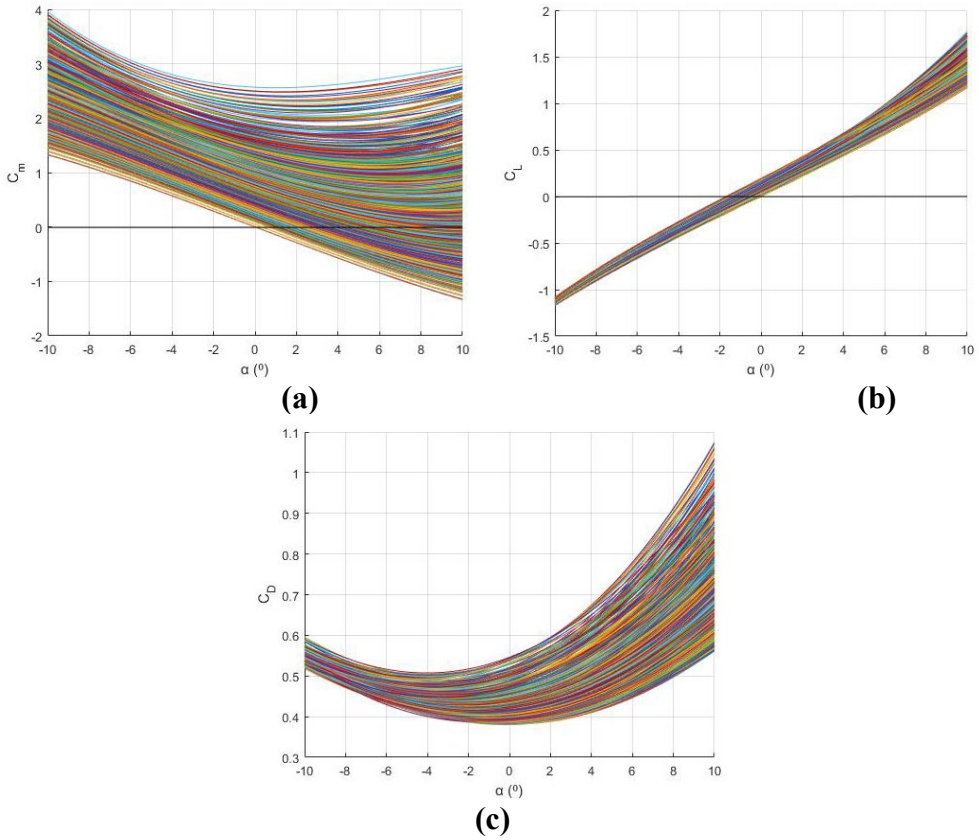

Fig. 39 Plots of a) C_m, b) C_L, and c) C_D vs. α for entire design space at Mach 2

From these data sets, the objective functions can be evaluated for each configuration that achieved trim condition. The first objective function value (Optimization Study 1: maximum *L/D* at respective trim angle) and second objective function value (Optimization Study 2: maximum C_m at $\alpha = 0°$) are plotted as a function of "bentness angle" θ, (Section 2.1, Fig. 3) in Fig. 40. By plotting the optimization goals with respect to θ, we can more easily understand how the bent body design space is related to the optimization goals as opposed to creating separate plots for each bending body parameter. Only 44% of all possible configurations were able to achieve trim within the $\alpha \leq 8°$ range investigated. The untrimmed configurations were neglected and, thus, discarded in the current optimization analysis. The distributions of both *L/D* and C_m for all configurations as a function of θ for each configuration are presented. From these plots, it is clear that both data sets reach respective maxima (shown in red) near the maximum θ value for the given trimmed configurations. How these maximums are reached by the PSO algorithm, as well as the aerodynamic characterization for these optimal configurations, are discussed in the following sections.

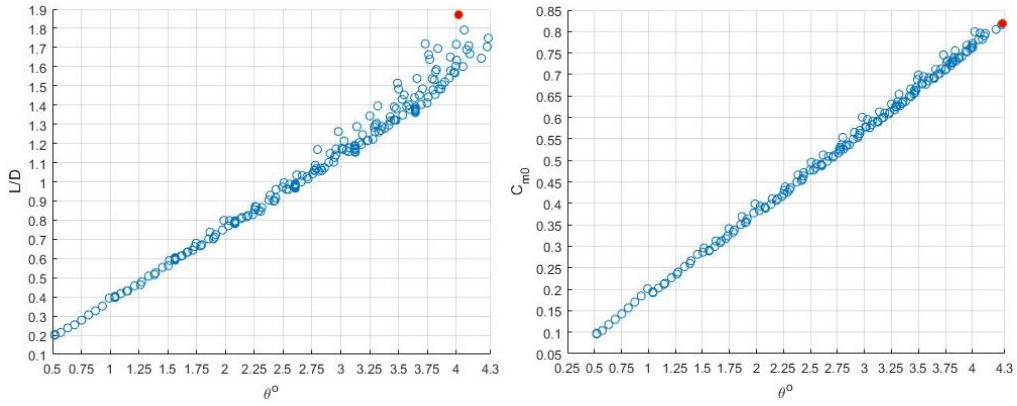

Fig. 40 Plot of *L/D* (left) and C_{m_0} (right) vs. θ for trimmed configurations at Mach 2

4.4 Particle Swarm Optimization Analysis

The PSO algorithm in MATLAB was effective at optimizing both maximum *L*/D and maximum C_{m_0} for trimmed configurations. Depicted in Figs. 41 and 42 are the geometric and aerodynamic parameters, respectively, that were found from each optimization study and are presented in Table 5. The results indicate that the optimization routine converges to similar "bentness" values of $\theta = 3.9°$ and $\theta = 4.1°$. However, as depicted in Figs. 41 and 42, there are subtle differences in the overall shape for each configuration. The optimal *L/D* configuration (Fig. 41) has a bend near the *c.g.* while the nose remains relatively straight, whereas the optimal C_{m_0}configuration (Fig. 42) has a small bend in the center body and a significant bend at the nose. Each optimal configuration is better than the other for their respective objective functions but achieve similar performance overall. This is an important observation to consider; there may be more than one design that can be used to accomplish maneuverability with bending body technology.

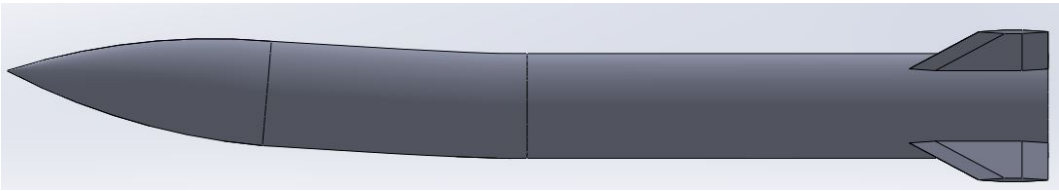

Fig. 41 Optimal L/D configuration

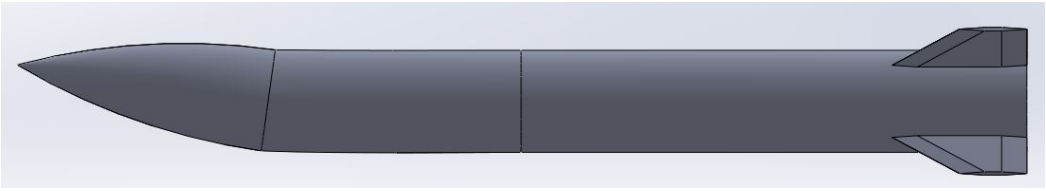

Fig. 42 Optimal C_{m_0} configuration

Table 5 Optimal configurations

Configuration	Φ_1 (°)	Φ_2 (°)	$Q1$ (mm)	Θ (°)	L/D	C_{m_0}	Trim α (°)
Optimal *L/D*	3	2	7	4.021	1.871	0.800	9.1
Optimal C_{m_0}	1	7	59	4.278	1.749	0.819	8.8

The optimal configurations were determined from the results of an in-depth analysis on optimization convergence characteristics. These assessments are made based on studying the average number of iterations, success rate at finding the true optimal configuration for a given execution, and resulting average score error. Ten optimization executions were performed for each objective function (maximum *L/D* and maximum C_{m_0}) for a given swarm size of 5, 10, 20, and 30 particles. These optimization metrics are summarized in Tables 6–9. An expected trend that emerges from analyzing the optimization studies show there is an increase in success rate and a decrease in score error as the swarm size increases. Subjectively, we can also see that an acceptable success rate is not achieved until the swarm size passes 10 particles. This phenomenon is observed in both PSO algorithms. For the in-house code, iterations increase with increasing swarm size, but for the MATLAB PSO algorithm, iterations decreased just slightly. Both algorithms were prohibited from passing 100 iterations.

Table 6 Optimization study metrics for maximum *L/D* at trim condition from in-house PSO algorithm

Swarm size	Average iterations	Success rate	Average *L/D*	Average *L/D* error
5	22	10%	1.652	11.7%
10	35	30%	1.737	7.2%
20	64	60%	1.811	3.2%
30	81	80%	1.846	1.3%

Table 7 Optimization study metrics for maximum *L/D* at trim condition from MATLAB PSO algorithm

Swarm size	Average iterations	Success rate	Average *L/D*	Average *L/D* error
5	26	10%	1.718	8.2%
10	26	0%	1.730	7.5%
20	23	40%	1.786	4.5%
30	24	50%	1.814	3.0%

Table 8 Optimization study metrics for maximum C_{m_0} from in-house PSO algorithm

Swarm size	Average iterations	Success rate	Average C_{m_0}	Average C_{m_0} error
5	15	0%	0.774	5.4%
10	73	50%	0.795	2.9%
20	55	50%	0.809	1.2%
30	78	60%	0.811	1.0%

Table 9 Optimization study metrics for maximum C_{m_0} from MATLAB PSO algorithm

Swarm size	Average iterations	Success rate	Average C_{m_0}	Average C_{m_0} error
5	27	10%	0.779	4.8%
10	28	60%	0.812	0.8%
20	25	70%	0.816	0.3%
30	25	90%	0.813	0.7%

To better understand the results of the optimization studies for both maximizing *L/D* and maximizing C_{m_0}, the parameter histograms of each optimization study can be analyzed. Beyond the success rate and the goal error, the histograms give us deeper insight into how well the optimization algorithms performed. Each histogram comprises the parameters of all the converged configurations from each swarm size for the respective study. By consolidating the data in this way, we are able to minimize the stochasticity of finite executions. The 12 histograms for these data sets are shown in Figs. 43–46. In Figure 43, we can see the presence of parameter probabilities for each parameter value from the maximum *L/D* routine executions using the in-house PSO algorithm. The parameters of the two optimal configurations found by the optimization studies are highlighted in each histogram in green and red columns for the optimal *L/D* and optimal C_{m_0} configurations, respectively. This is done to show that for each objective function, the parameters of the optimal configuration found using the alternate objective function have a high probability of occurring.

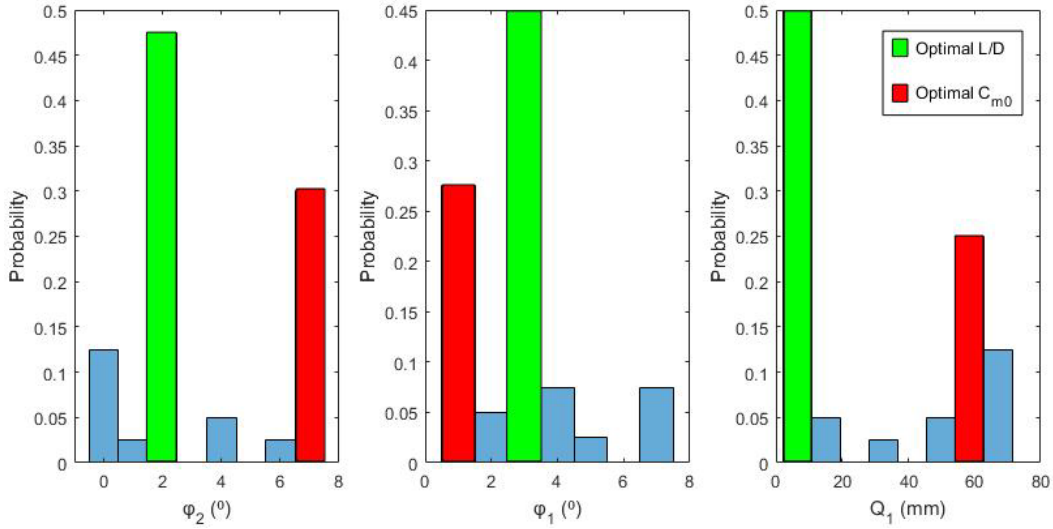

Fig. 43 Parameter probability histograms for maximum *L/D* from in-house PSO algorithm

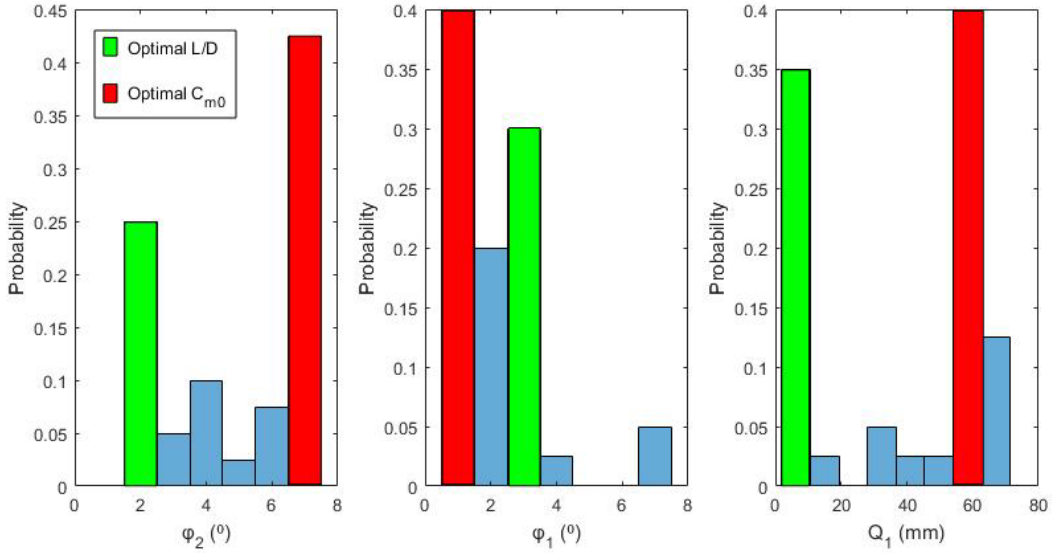

Fig. 44 Parameter probability histograms for maximum *L/D* from MATLAB PSO algorithm

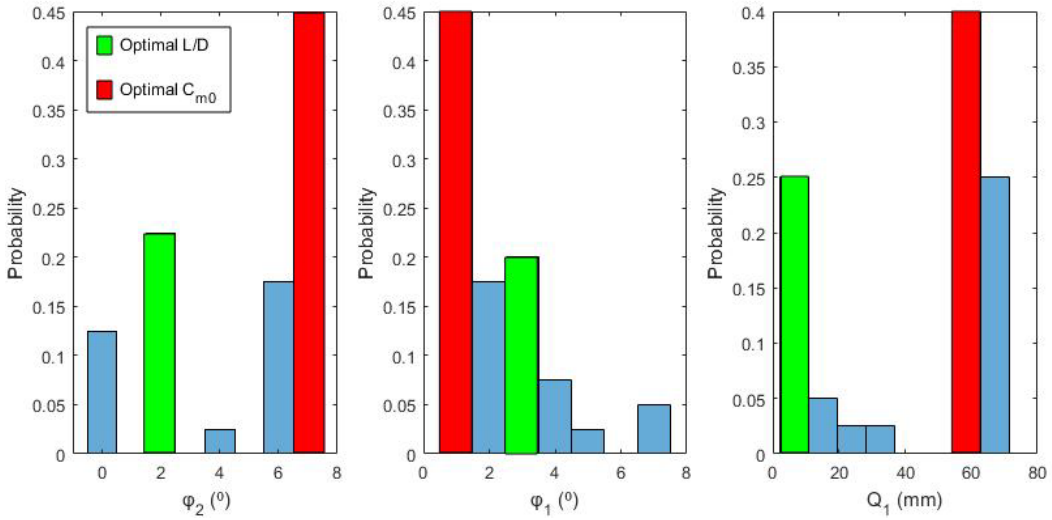

Fig. 45 Parameter probability histograms for maximum C_{m_0} at α = 0° from in-house PSO algorithm

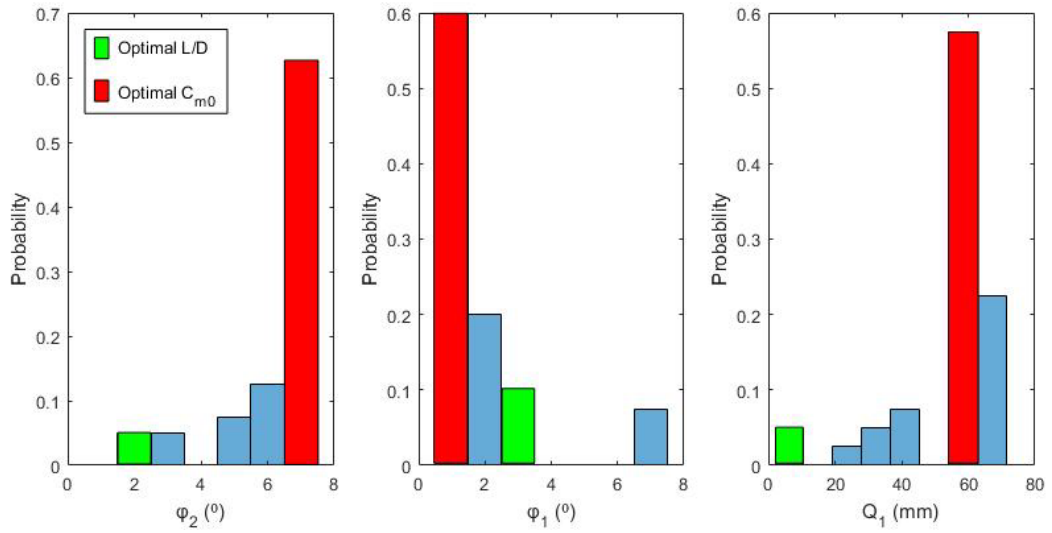

Fig. 46 Parameter probability histograms for maximum C_{m_0} at α = 0° from MATLAB PSO algorithm

The first check we can make is that each histogram exhibits a high probability of the optimal configuration for the optimization study (i.e., the optimal *L/D* configuration for optimizing *L/D*). As an interesting result, there is also a rather high concentration of the other optimal configuration in each figure (excluding Fig. 46). Explained more explicitly, the parameter histograms generated by the optimization studies for maximizing *L/D* also exhibit a high probability of the parameters that characterize the optimal C_{m_0} configuration and vice versa. Among general observations, there are also subtle observations worth noting. In Fig. 44 we

see the optimal C_{m_0} configuration is present in the maximum *L/D* study with greater probability. While unexpected, it is important to remember that both optimal configurations attain similar performance in both objective functions. So while converging to a suboptimal configuration with a high probability is not ideal, it is not unusual for a heuristic, especially when the suboptimal configuration is very close to the optimal configuration in performance. As another subtle observation, neither expected nor unexpected, the optimal *L/D* configuration has relatively reduced probability when maximizing C_{m_0} with the MATLAB PSO algorithm (Fig. 46). This observation is relative to Figs. 43–45, especially Fig. 45. There is no causal reason to expect a relatively high probability (with respect to itself) of this suboptimal in this optimization study, but since it was found in all other cases, it is unusual.

After completing our analysis of the parameter histograms, we can also analyze results histograms of all four optimization studies, shown in Figs. 47 and 48. Generally, both algorithms performed well optimizing each objective function (possibly excluding the MATLAB PSO algorithm's optimization of maximum *L/D* at trimmed condition.) We can see the optimal result was generally found with the highest probability, and suboptimal results were found with exponentially decreasing probability as the result decreases in objective function value. Additionally, it appears the algorithms found greater success optimizing C_{m_0} in contrast to optimizing *L/D*. This observation is supported by the greater probability of converging to the optimal configuration in contrast to optimizing for *L/D*. This could imply that optimizing C_{m_0} was easier than optimizing *L/D*. Finally, we can note the consistency between the MATLAB PSO algorithm results histogram in Fig. 47 and the parameter histogram in Fig. 44. While there is not a perfect mapping of the parameter probabilities to the results probabilities, each histogram is evidential support of the other.

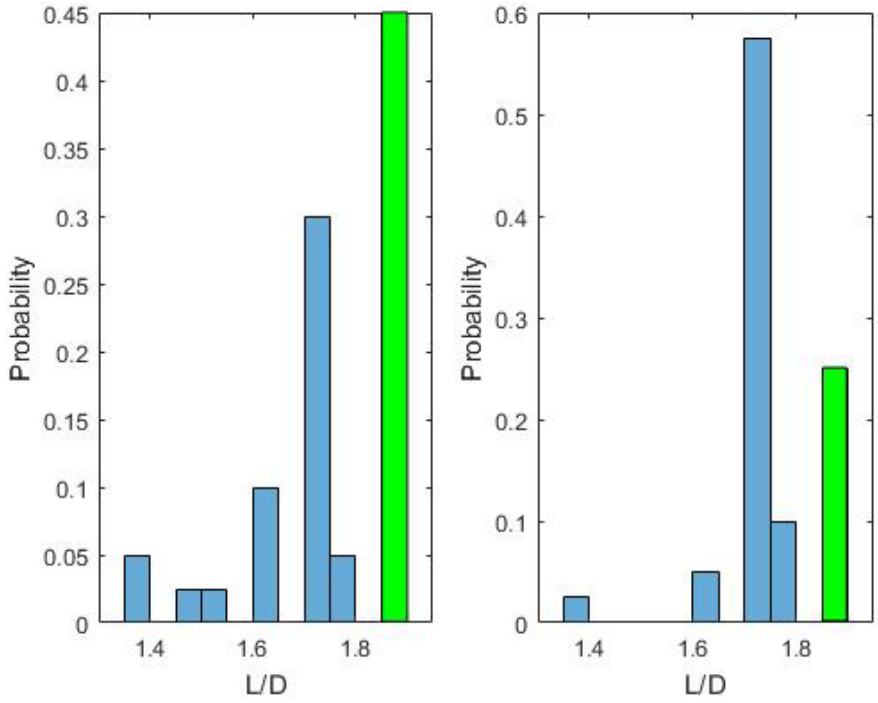

Fig. 47 ***L/D*** **results probability histograms from in-house PSO algorithm (left) and MATLAB PSO algorithm (right)**

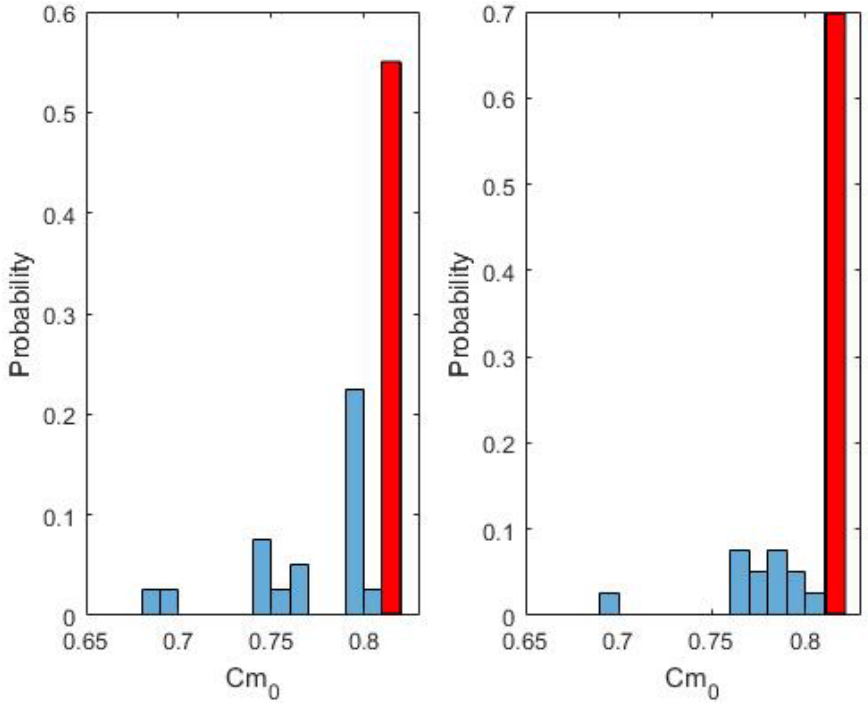

Fig. 48 C_{m_0} **results probability histograms from in-house PSO algorithm (left) and MATLAB PSO algorithm (right)**

4.5 Optimized Bent Body Projectile Analysis

The data for the optimal configurations as well as three canard configurations, in the form of α-sweeps, are displayed in Figs. 49–52 and summarized in Table 10. The data for the optimal configurations were curve-fitted to interpolate the trim angle location and are plotted in the figures along with the raw data. The optimal configurations for each respective objective function result in similar aerodynamic characteristics. Both configurations behave similarly for C_m (Fig. 49), reaching trim conditions at 8.8° and 9.1°. Overall, the aerodynamics of the optimal configurations behave linearly until approximately $\alpha = 4°$. At $\alpha > 4°$, the C_m of the bent body becomes nonlinear. At all α, the optimal configurations generate significantly larger C_m, as well as C_{m_0}, compared with the canard configurations. The bent body configurations have double the C_{m_0} value compared with the $\delta = 10°$ canard configuration. This indicates the bent body configuration has the potential for more maneuver authority than the $\delta = 10°$ canard-controlled configuration. The optimal C_{m_0}configuration features a significantly bent nose as compared to the moderately bent body of the *L/D* configuration but the "bentness" parameter, θ is comparable. The aerodynamic parameters are summarized in Table 10.

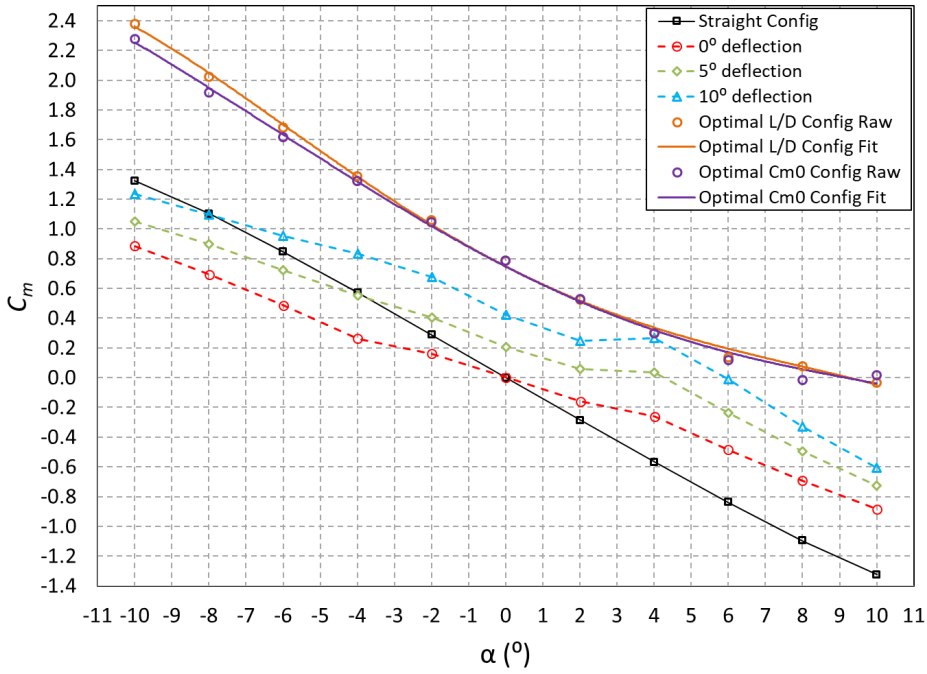

Fig. 49 C_m vs. α for optimal configurations and canard configurations at Mach 2

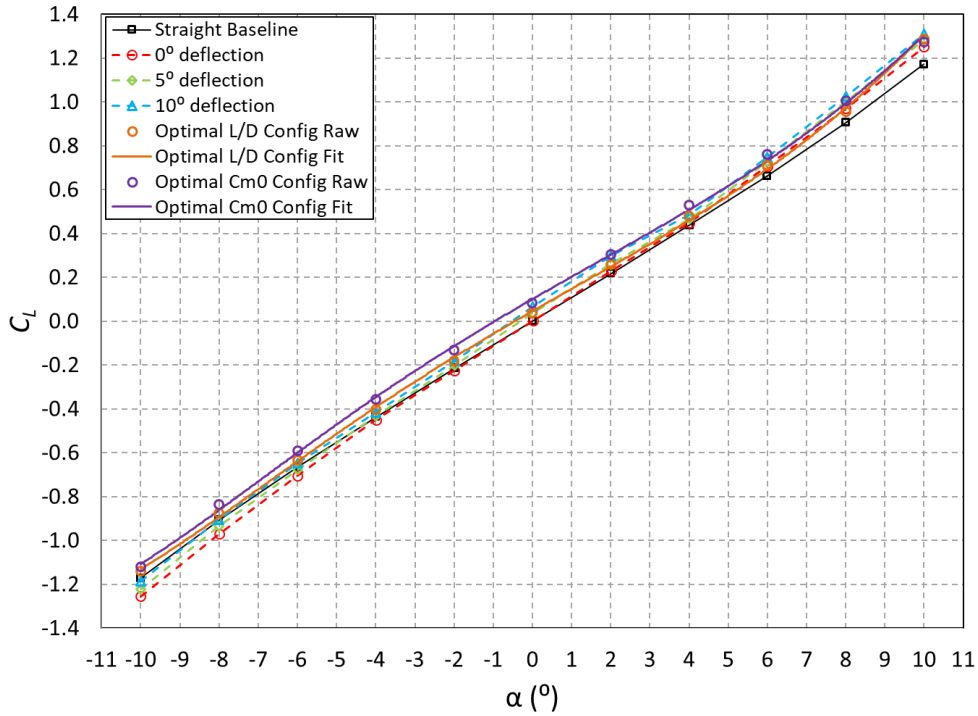

Fig. 50 C_L **vs.** α **for optimal configurations and canard configurations at Mach 2**

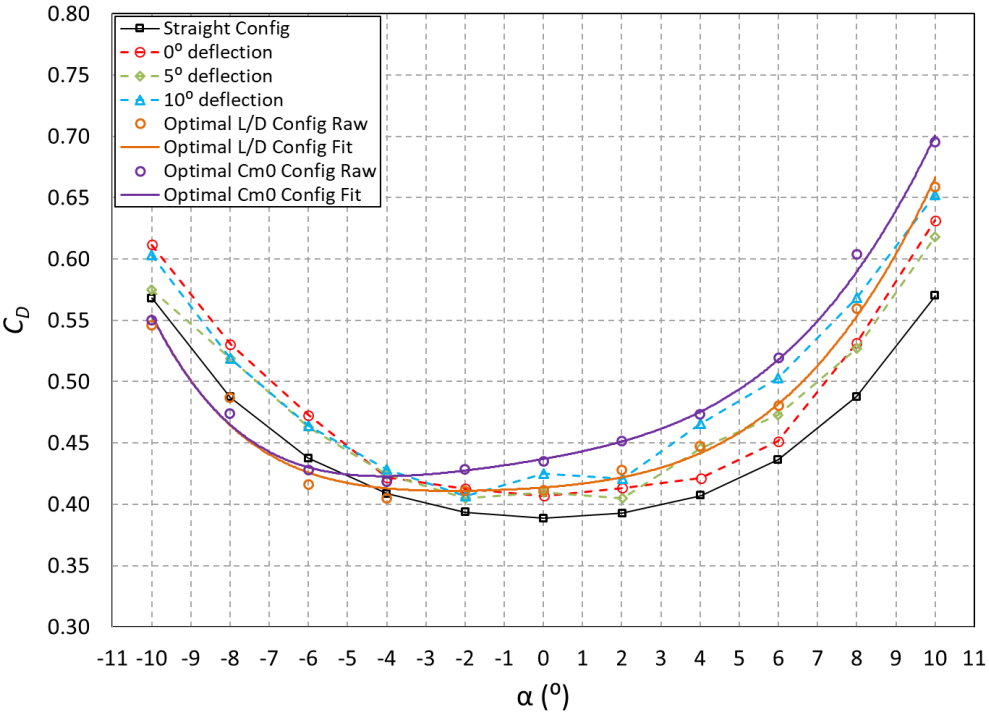

Fig. 51 C_D **vs.** α **for optimal configurations and canard configurations at Mach 2**

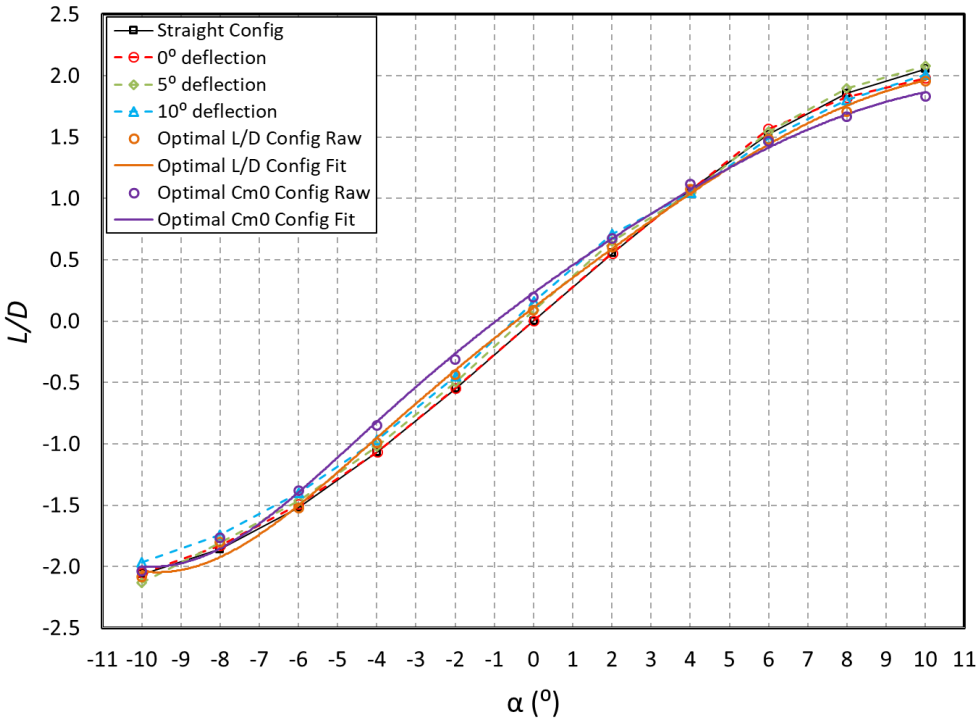

Fig. 52 ***L/D*** **vs.** α **for optimal configurations and canard configurations at Mach 2**

Table 10 Comparison of significant aerodynamic metrics between the optimal bent body configuration, the canard configurations and the baseline configuration

Configuration	Trim α (°)	C_{m_0}	C_L at trim	C_D at trim	L/D at trim
Baseline	0.0	0.0	0.0	0.380	0.0
$\delta = 0°$ Canard	0.0	0.0	0.0	0.395	0.0
$\delta = 5°$ Canard	3.3	0.207	0.405	0.425	0.953
$\delta = 10°$ Canard	5.5	0.423	0.695	0.496	1.401
Optimal L/D	9.1	0.800	1.143	0.611	1.871
Optimal C_{m_0}	8.8	0.819	1.113	0.636	1.749

There is little difference in C_L between the optimal bent body and the canard configurations (Fig. 50). At the highest α, the bent body configurations provide about the same lift as the $\delta = 10°$ canard configuration. However, there are significant differences in the drag profiles of each configuration (Fig. 51). At $\alpha = 0°$ the bent body configurations have about a 4%–13% increase in C_D. At

positive α the bent body configurations have comparable values of C_D as the deflected canard configurations. At negative α, the bent body configurations have lower C_D values than the canard configurations ($\alpha \leq -4°$) and the unbent configuration ($\alpha \leq -5°$). Moreover, the optimal C_{m_0} configuration has a larger C_D value than the optimal *L/D* configuration, indicating that the larger deflection of the nose (Table 5) will lead to a small amount increased drag (6% over the optimal *L/D* value). Synthesizing the C_L and C_D data into a single value, we can plot *L/D* (Fig. 52). Much like C_L, *L/D* appears to be mostly linear and C_D seems to modulate the value of *L/D*. Studying the plot we can see an inflection point seems to occur at $\alpha = 4°$. The inflection point marks the α where bending body technology is no longer providing greater increase in lift for greater increase in drag. However, if we remember from Fig. 49, the bending body configurations trim at a higher α than the canard configurations and are therefore providing significantly more lift at trim (about 57% over the $\delta = 10°$ canard configuration).

The performance of control actuators can also be quantified by calculating the incremental differences in the coefficients as compared with the undeflected configuration, which is the standard AFF body-fin configuration in this case. These increments are defined as ΔC_D, ΔC_L, and ΔC_m and are presented in Figs. 53–55. The C_m increments, shown in Fig. 53, indicate a much larger value for the bent body configurations over most of the angle-of-attack range. As the bent configurations can have more positive C_m than the canard configurations for $\alpha \leq 0°$, the C_m increments are nearly symmetric, while those for the canard configurations are antisymmetric about $\alpha = 0°$. The higher C_m increments for the bent configurations lead to higher trim α than the canard configurations (Table 10). This results in the higher *L/D* values at trim and increased maneuverability. The *L/D* at trim for the optimal *L/D* bent configuration is 34% higher than the *L/D* at trim for the $\delta = 10°$ canard configuration.

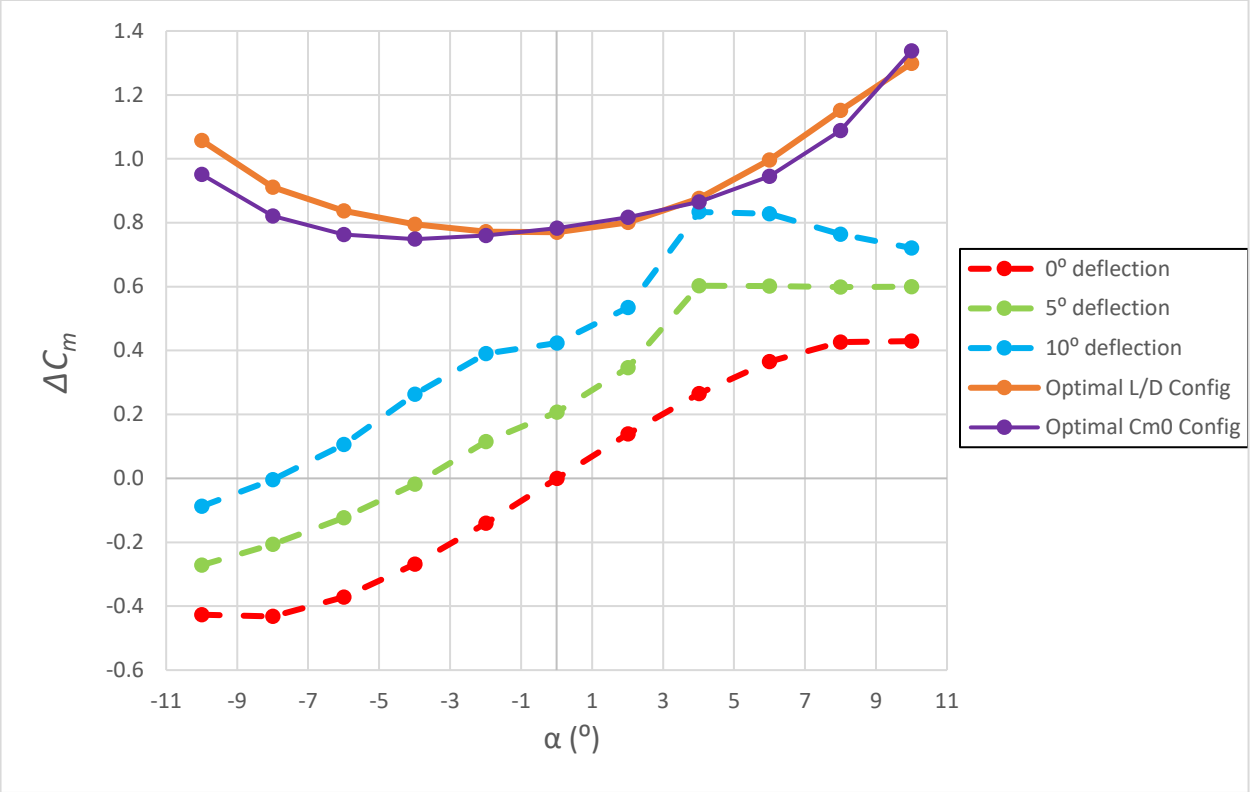

Fig. 53 C_m increment for canard configurations and optimal bent configuration

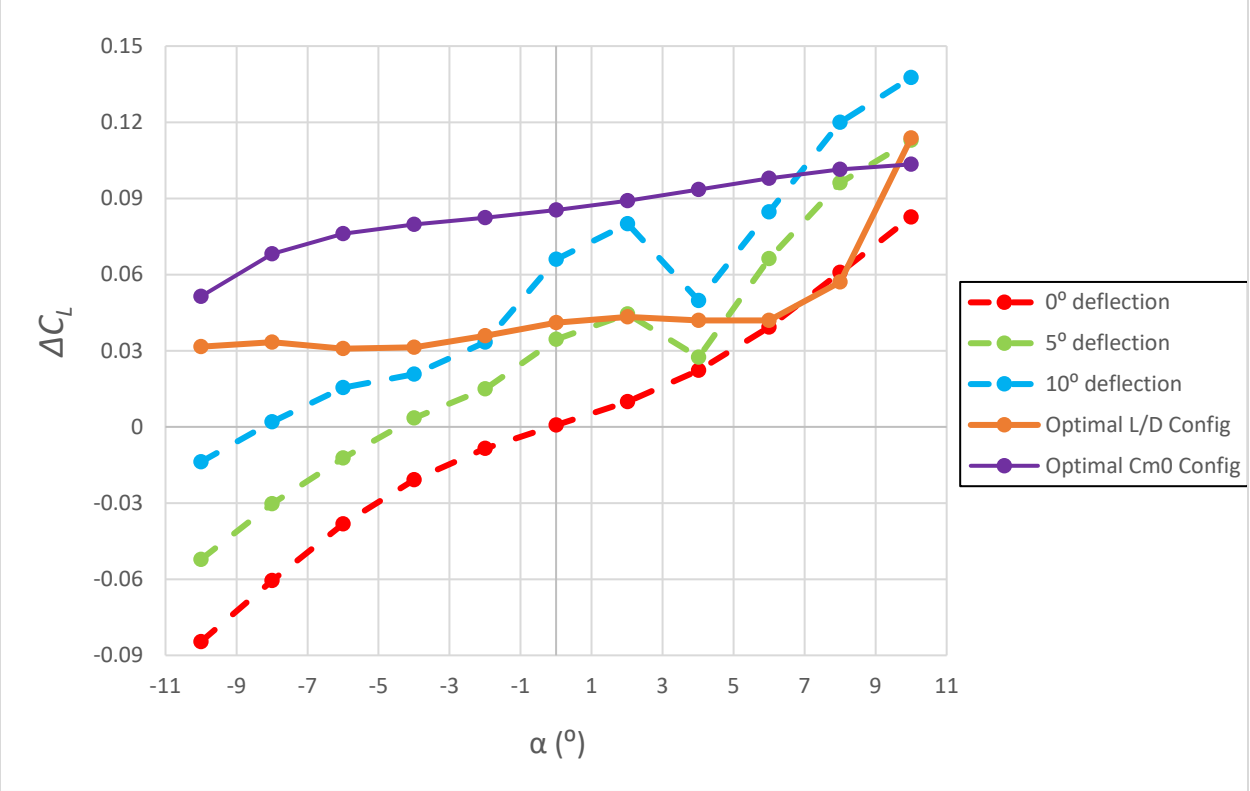

Fig. 54 C_L increment for canard configurations and optimal bent configuration

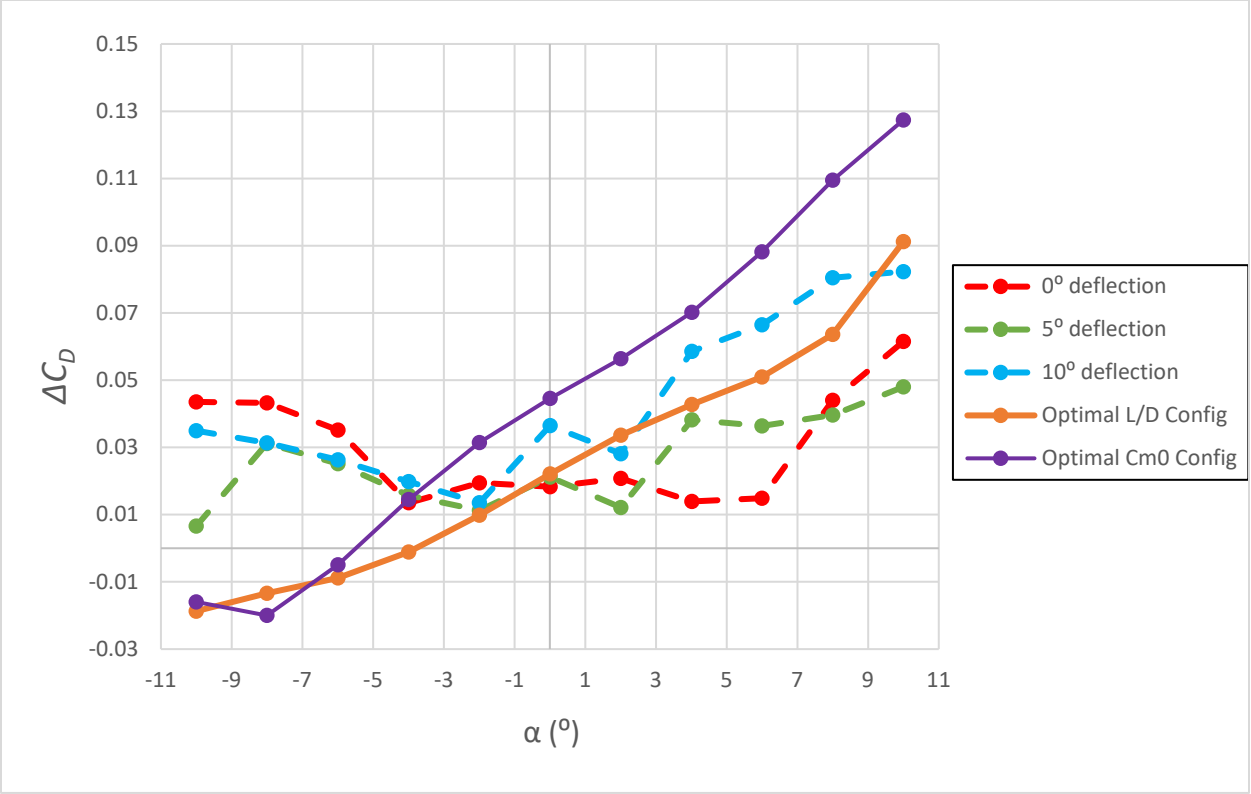

Fig. 55 C_D increment for canard configurations and optimal bent configuration

The C_m increments, shown in Fig. 53, indicate a much larger value for the bent body configurations over most of the angle-of-attack range. As the bent configurations can have more positive C_m than the canard configurations for $\alpha \leq 0°$, the C_m increments are nearly symmetric, while those for the canard configurations are antisymmetric about $\alpha = 0°$. The higher C_m increments for the bent configurations lead to higher trim α than the canard configurations (Table 10). This results in the higher *L/D* values at trim and increased maneuverability. The *L/D* at trim for the optimal *L/D* bent configuration is 34% higher than the L/D at trim for the $\delta = 10°$ canard configuration.

Figure 54 shows the ΔC_L curves for the canard configurations. The optimal C_{m_0} configuration provides about the same C_L increment as the $\delta = 10°$ canard configuration. The optimal *L/D* configuration provides similar C_L as that of the lower canard deflection configurations until $\alpha = 10°$, where it provides comparable C_L as the optimal C_{m_0} configuration. This indicated a more bent nose provides a higher C_L increment than the more subtle bend at the rearward section, with θ value being comparable. However, the optimal *L/D* configuration has lower C_D increment (Fig. 55). The C_D increment for the bent body configurations are larger than the configurations with canards; however, the canards are always deployed while the high-drag bent body configuration is only present during the

maneuver. Even the nonmaneuvering, $\delta = 0°$ configuration has significant C_D increment for $\alpha > 7°$. The optimal *L/D* configuration has a C_D increment value that falls between the 5° and 10° canard deflection cases, increasing above the latter at $\delta = 10°$. The optimal C_{m_0} configuration has the highest C_D increment of all configurations for $\alpha > -4°$. This configuration has the most-bent nose section, which likely produces the largest wake-like flow leading to increased pressure drag contribution.

Contours of Mach number and pressure coefficient for both optimal bent configurations and the $\delta = 10°$ canard configuration are presented in Figs. 56 and 57, respectively. At $\alpha = 0°$, the canard configuration (Fig. 56c) shows the typical flow characteristics in supersonic flow: a symmetric attached oblique shock at the nose and expansion waves at the ogive–cylinder body junction. Some evidence of canard trailing vortices and wake flow is observed as regions of low surface pressure behind the canards. In contrast, the bent body configurations (Fig. 56a and b) show an asymmetric oblique shock that provides the majority of the lift increment and a recompression shock at the location where the bent section meets the straight aft body. No significant differences are observed in the projectile wake. At increased angle of attack (Fig. 57) these flow features are still present and are increased in intensity. The canard configuration (Fig. 57c) bow shock is now also asymmetric and leads to lift provided by the projectile body. The low-pressure regions along the side of the bent body configurations (Fig. 57b and c) indicate that a pair of symmetric, co-rotating vortices have formed over the ogive section, as the effective angle of attack of the nose section is now greater than 14°. Symmetry of these vortices is indicated since no side force was generated. Differences in the projectile wake flow between the bent body configurations and the canard configuration are now also observed, which is due to interaction of the body vortices and other effects of the flow in the wake of bent forward section.

From the analysis of the aerodynamic coefficients of the two optimal bent configurations, it is observed that they are similar in aerodynamic performance while having a distinct difference in "local" shape. Both have similar C_m increments. The optimal *L/D* configuration has slightly higher *L/D* at trim, owing to lower C_D increment. The overall "bentness" parameter, θ, appears to be the significant shape parameter for the conditions of this study. The configuration chosen for implementation may depend on other design considerations, such as requirements on actuator location, payload location, and seeker configuration. It is advantageous to have the capability to reach equivalent maneuverability via the two different bent body configurations.

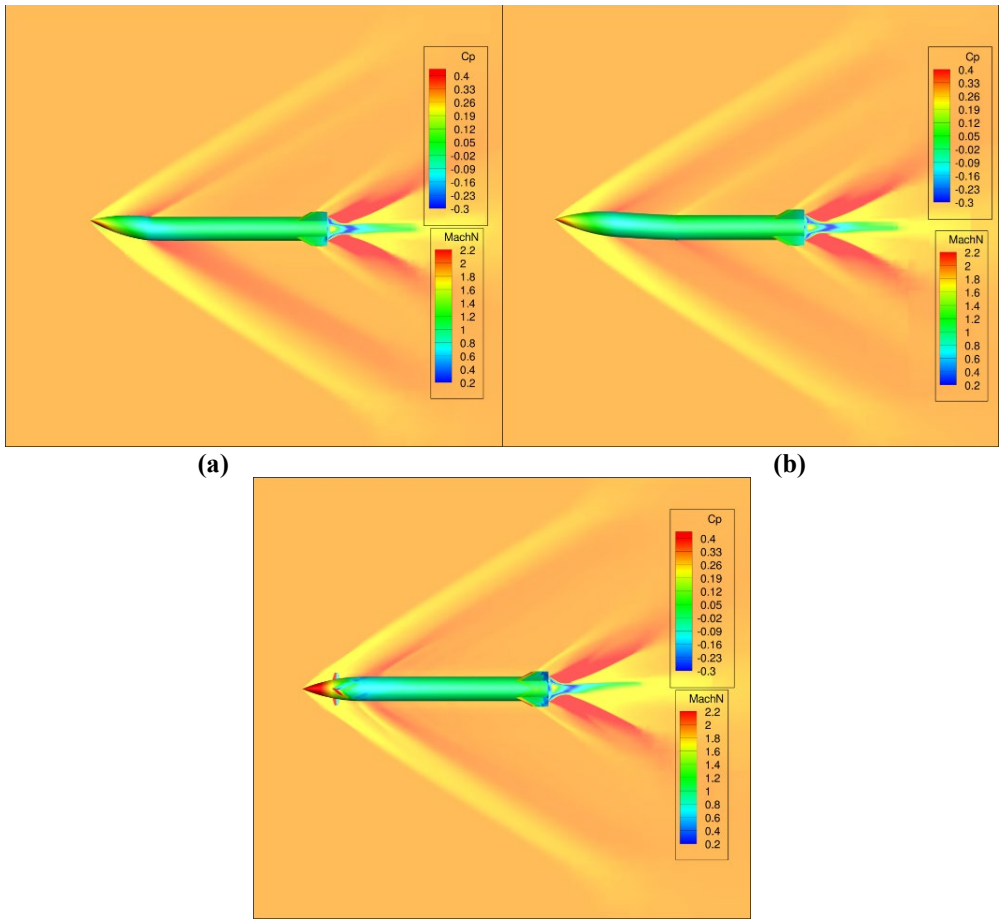

Fig. 56 Mach contours on symmetry plane and surface pressure coefficient contours of the a) optimal C_{m_0}, b), optimal *L/D*, and c) and $\delta = 10°$ canard configurations at Mach 2 and $\alpha = 0°$

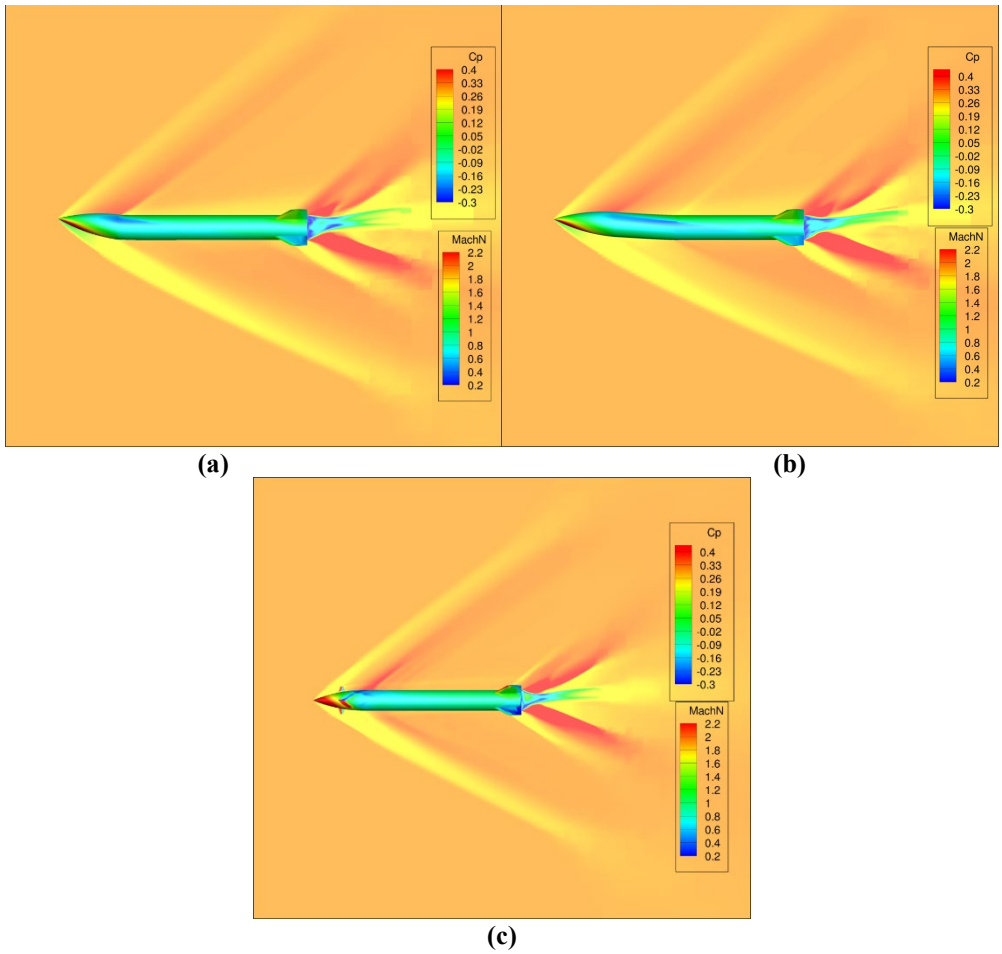

Fig. 57 Mach contours on symmetry plane and surface pressure coefficient contours of the a) optimal C_{m_0}, b) optimal *L/D*, and c) $\delta = 10°$ canard configurations at Mach 2 and respective trim angle of attack

Taking some of the information from Table 10, a preliminary estimation of the dynamic rates for different configurations can be calculated to provide an indicator of the potential maneuver authority of each configuration. This is achieved by using C_L and C_{m_0} to obtain the corresponding lateral and pitch accelerations. The lateral acceleration comes from Newton's Second Law of Motion and the pitch acceleration comes from Euler's Rotation Equation. These accelerations are determined using mass properties obtained from aerodynamic range tests.[38] The mass properties and conditions used to perform the calculations are shown in Table 11, and the resulting metrics are shown in Table 12. Naturally the baseline and $\delta = 0°$ canard configuration are omitted due to their zero-valued aerodynamic coefficients, as shown in Eqs. 2 and 3.

$$a = \frac{C_L \bar{q} \left(\frac{1}{4}\pi D^2\right)}{m}. \tag{2}$$

$$\dot{\omega} = \frac{C_{m_0} \bar{q} \left(\frac{1}{4}\pi D^2\right) D}{I_{yy}}. \tag{3}$$

Table 11 Air Force Finner mass properties

Density (kg/m^3)	Temperature (K)	Specific gas constant (J/(kg·K))	Mach number	Diameter (m)	Reference area (m^2)	Pitch moment of inertia (kg· m^2)	Mass (kg)
1.225	288.15	287.058	2	0.03	0.00071	0.00486	0.664

Table 12 Estimated dynamic rates for maneuver configurations

Configuration	C_L at α_{trim}	Lateral acceleration (g)	C_{m_0}	Pitch acceleration (rad/s^2)
$\delta = 5°$ canard	0.405	11.3	0.207	232.0
$\delta = 10°$ canard	0.695	19.4	0.423	474.2
Optimal *L/D*	1.143	31.8	0.800	896.8
Optimal C_{m_0}	1.113	31.0	0.819	918.1

In Table 12 the expected trends are observed. As C_L at trim increases, lateral acceleration increases, and as C_{m_0} increases, pitch acceleration increases. The minor differences in acceleration between the two optimal bent body configurations are consistent with the minor differences in C_L and C_m increment, indicating each configuration should have similar maneuver authority. However, both optimal bent body configurations provide significant more maneuver authority than the $\delta = 10°$ canard configuration: approximately 50% more lateral acceleration and double the pitch acceleration. This is another indicator of the potential advantage of bent body control over canard control.

5. Summary and Conclusions

A numerical study was completed to investigate the feasibility of using a bending body projectile as a possible maneuver mechanism for a supersonic projectile. The baseline configuration was the AFF straight body, which was simulated at both Mach 2 and Mach 3. The bent body configurations were generated with two bends, one at the ogive–cylinder intersection and the other between intersection and the center of gravity. Both bending angles were only allowed in the same direction. CFD^{++} and Cart3D simulation results were validated for the baseline AFF configuration using previously obtained experimental data and compared to Missile DATCOM predictions.

Thirty randomly chosen bent body configurations were investigated with CFD^{++} at Mach 2 and Mach 3. C_D varied significantly among configurations, Mach number and α. The projected area was the significant driver, as the projectile was only bent one direction; configurations with larger bends had greater projected area and thus greater C_D. C_L variation was likely minimized by the adverse effect of leeside separation causing a higher pressure and thus reducing the lift that can be produced with increasing bending angles. C_m showed significant variation with α at both Mach numbers. These variations could be separated into four regimes: a shift in C_{m_0} (minimal change in slope), decreasing slope of C_m with increasing α, varying slope in C_m such that a local minimum is obtained, varying slope in C_m such that both a local minimum and local maximum occur. Due to the greater stability of the AFF at Mach 2, these four regimes could be more easily identified; one case was selected for further investigation in each regime. At Mach 2 nearly one-third of the configurations could reach a trimmed condition (all were in the first two regimes), while only 1 model of the 30 investigated could reach a trimmed condition at Mach 3. These conclusions are based on the limited angle of attack range investigated, $\alpha \leq 10°$; it is possible that some configurations may trim at a higher α.

Four bent body configurations were down-selected for further analysis and comparison with Cart3D simulations, as it was determined that performing the optimization study with the full Navier–Stokes CFD solver would be too computationally intensive. Comparison of Cart3D to the CFD++ for these four cases demonstrated that Cart3D could be used to efficiently simulate the flow around the bent body configurations while obtaining adequate prediction of the aerodynamic coefficients. Comparison of the flowfield for the bent body configurations revealed that body-shed vortices form on the ogive even at moderate projectile α (<10°) because the effective angle of attack of the bent ogive section is greater (≥14°). These vortices lead to differences in the projectile wake flow as compared with the canard configurations.

In conjunction with the aerodynamic coefficients generated by Cart3D, a PSO algorithm was used to find the optimum bend angles and location. Two objective functions were investigated, one seeking to maximize *L/D* and the other to maximize C_{m_0}, while also requiring that the configuration reach the trimmed condition. The optimization routine for each objective function converged to a different configuration, one with a large bending angle at the nose and the other with a smaller angle bend closer to the *c.g.* and nearly no bend at the nose. However, the two configurations had similar *L/D*, C_{m_0}, trim α, and a similar "bentness" angle, θ.

The aerodynamic characteristics of the optimal designs were further analyzed and compared with a conventional static deflected canard variant of the AFF. Larger C_m increments were found for either of the bent configurations, leading to higher trim α than the canard configurations. This results in the higher *L/D* values at trim and increased potential maneuverability. The *L/D* at trim for the optimal *L/D* bent configuration was 34% greater than the *L/D* at trim for the $\delta = 10°$ canard configuration. Similarly, the optimal C_{m_0} bent configuration was 94% greater than the C_{m_0} for the $\delta = 10°$ canard configuration. Estimates of lateral and pitch acceleration also indicated significant potential increased maneuver authority over canard configuration. Flight trajectory simulations of the optimal configurations will need to be completed using the aerodynamic models generated using Cart3D to quantify the maneuver authority of the bent body configurations.

6. References

1. Fresconi F, Brown G, Celmins I, DeSpirito J, Ilg M, Maley J, Magnotti P, Scanlan A, Stout C, Vazquez E. Very affordable precision projectile technology development and flight demonstrations. Aberdeen Proving Ground (MD): Army Research Laboratory (US); 2011 Mar. Report No.: ARL-TR-5460.

2. Fresconi FE, Harkins T. Experimental flight characterization of asymmetric and maneuvering projectiles from elevated gun firings. Journal of Spacecraft and Rockets. 2012;49(6):1120–1130.

3. Fresconi FE. Guidance and control of a projectile with reduced sensor and actuator requirements. Journal of Guidance, Control, and Dynamics. 2011;34(6):1757–1766.

4. Fresconi F, Celmins I, Ilg M, Maley J. Projectile roll dynamics and control with a low-cost skid-to-turn maneuver system. Journal of Spacecraft and Rockets. 2014;51(2):624–627.

5. Paul JL, Silton SI. Influence of bending locations and angles on the aerodynamic performance of a bent body projectile. Proceedings of the AIAA SciTech Forum; 2018 Jan; Kissimmee, FL. Paper No.: AIAA 2018-1269.

6. Youn EB, Silton SI. Numerical study on bending body projectile aerodynamics. Proceedings of the 34th Applied Aerodynamics Conference; 2016 June; Washington, DC. Paper No.: AIAA 2016-4331.

7. Rockwell D. Vortex-body interactions. Ann Rev Fluid Mech. 1998 Jan:30199–30229.

8. McDaniel MA, Evans C. The effect of tail fin parameters on the induced roll of a Canard-controlled missile. Proceedings of the 28th AIAA Applied Aerodynamic Conference; 2010 June; Chicago, IL. Paper No.: AIAA-2010-4226.

9. Lesieutre DJ, Quijano O. Studies of vortex interference associated with missile configurations. Proceedings of the 52nd Aerospace Sciences Meeting; 2014 Jan; National Harbor, MD. Paper No.: AIAA-2014-0213.

10. Mendenhall MR, Perkins Jr SC, Lesieutre DJ. Vortex cloud model for body vortex shedding and tracking. Tactical missile aerodynamics: prediction methodology. In: Mendenhall MR, editor. Progress in astronautics and aeronautics, Washington (DC): AIAA; 1992. p. 225–285

11. Nygaard TA, Meakin RL. Aerodynamic analysis of a spinning missile with dithering canards. Journal of Spacecraft and Rockets. 2004;41(5):726–734.

12. Beresh SJ, Henfling JF, Spillers RW. Planar velocimetry of a fin trailing vortex in subsonic compressible flow. AIAA Journal. 2009;47(7):1730–1740.

13. Beresh SJ, Smith JA, Henfling JF, Grasser TW, Spillers RW. Interaction of a fin trailing vortex with a downstream control surface. Journal of Spacecraft and Rockets. 2009;46(2):318–328.

14. Beresh SJ, Henfling F, Spillers RW. Turbulence of a fin trailing vortex in subsonic compressible flow. AIAA Journal. 2012;50(11):2609–2622.

15. Barnes CJ, Visbal MR, Huang PG. Analysis of streamwise-oriented vortex interactions for two wings in close proximity. Physics of Fluids. 2015;27(1):015103.

16. Silton SI, Fresconi F. Effect of canard interactions on aerodynamic performance of a fin-stabilized projectile. Journal of Spacecraft and Rockets. 2013;52(5):1430–1442.

17. Silton SI, Coyle CJ. Effect of canard deflection for roll control on fin performance of a fin-stabilized projectile. Proceedings of the 54th AIAA Aerospace Sciences Meeting; 2016 Jan; San Diego, CA. Paper No.: AIAA 2016–0309.

18. Silton SI, Coyle CJ. Effect of canard deflection on fin performance of a fin-stabilized projectile. Proceedings of the 33rd AIAA Applied Aerodynamics Conference; 2015 Jan; Dallas, TX. Paper No.: AIAA 2015–2586.

19. DeSpirito J. CFD validation of interaction of fin trailing vortex with downstream control surface in high subsonic flow. Proceedings of the 54th AIAA Aerospace Sciences Meeting; 2016 Jan; San Diego, CA. Paper No.: AIAA 2016-1546.

20. Blair AB. Wind tunnel investigation at supersonic speeds of a canard controlled missile with fixed and free-rolling tail fins. Hampton (VA): NASA; 1978 Sep. NASA Technical Paper 1316.

21. Ericsson LE, Reding JP. Steady and unsteady vortex-induced asymmetric loads on slender bodies. Journal of Spacecraft and Rockets. 1981;18(2):97–109.

22. Thomson KD. The use of a deflectable nose on a missile as a control device. Salisbury (England): Defence Research Centre Salisbury; 1981 May. Report No.: WSRL-0211-TR.

23. Thomson KD. Wind tunnel tests on a tube-launched missile configuration with a deflectable nose control and a novel wrap-around fin stabilizer. Salisbury (England): Defence Research Centre Salisbury; 1983 Aug. Report No.: WSRL-0327-TR.

24. Landers MG, Hall LH, Auman LM, Vaughn ME. Deflectable nose and canard controls for a fin-stabilized projectile at supersonic and hypersonic speeds. Proceedings of the 21st Applied Aerodynamic Conference; 2003 June. Paper No.: AIAA 2003-3805.

25. Vaughn ME, Auman LM. Assessment of a productivity-oriented CFD methodology for designing a hypervelocity missile. Proceedings of the 21st Applied Aerodynamic Conference; 2003 June. Paper No.: AIAA-2003-3937.

26. Shoesmith B, Birch T, Mifsud M, Meunier M, Shaw S. CFD analysis of a supersonic projectile with deflectable nose control. Proceedings of the 3rd Flow Control Conference; 2006 June. Paper No.: AIAA-2006-3200.

27. Li J, Wray TJ, Agarwal RK. Shape optimization of supersonic bodies to reduce sonic boom signature. Proceedings of the 34th AIAA Applied Aerodynamics Conference; 2016 June; Washington, DC; Paper No.: AIAA 2016-3432.

28. Upender KK, Nguyen NT. Lift optimization study of a multi-element three-segment variable camber airfoil. 34th AIAA Applied Aerodynamics Conference, 2016 June 13–17, Washington, DC. AIAA 2016-3569.

29. Xiaoming F, Yufei Z, Chen H. Transonic nacelle aerodynamic optimization based on hybrid genetic algorithm. Proceedings of the 34th AIAA Applied Aerodynamics Conference; 2016 June; Washington, DC; Paper No.: AIAA 2016-3833.

30. Koreanschi A, Gabor OS, Acotto J, Botez RM, Mamou M, Mebarki Y. A genetic algorithm optimization method for a morphing wing tip demonstrator validated using infra-red experimental data. Proceedings of the 34th AIAA Applied Aerodynamics Conference; 2016 June; Washington, DC; Paper No.: AIAA 2016-4037.

31. Kennedy J, Eberhart R. Particle swarm optimization. IEEE International Conference on Neural Networks. 1995;4:1942–1948.

32. Vasile JD, Celmins I, Nelson B. Aerodynamic design optimization of control mechanisms for a subsonic, small diameter munition. Proceedings of the AIAA SciTech Forum; 2018 Jan; Kissimmee, FL. Paper No.: AIAA 2018-1654.

33. Eberhart R, Kennedy J. A new optimizer using particle swarm theory. Proceedings of the 6th International Symposium on Micro Machine and Human Science; 1995.

34. Venter G, Sobieszczanski-Sobieski J. Particle swarm optimization. Proceedings of the 43rd AIAA/ASME/ASCE/AHS/ASC Structures, Structural Dynamics, and Materials Conference; 2002. AIAA Paper No. AIAA 2002-1235.

35. Shi Y, Eberhart R. A modified particle swarm optimizer. Proceedings of the IEEE International Conference on Evolutionary Computation; 1998. p. 69–73.

36. Nickabadi A, Ebadzadeh M, Safabakhsh R. A novel particle swarm optimization algorithm with adaptive inertia weight. Applied Soft Computing. 2011;11(4):3658–3670.

37. Qin Z, Yu F, Shi Z, Wang Y. Adaptive inertia weight particle swarm optimization. Proceedings of the 8th International Artificial Intelligence and Soft Computing Conference; 2006 June. p. 450–459.

38. Dupuis AD, Hathawa W. Aeroballistic range tests of the Air Force Finner reference projectile. Valcartier (Canada): Defense R&D Canada; 2002 May. Report No.: TM 2002–008.

39. West KO. Comparison of free flight spark range and wind tunnel test data for a generic missile configuration at Mach numbers from 0.6 to 2.5. Eglin Air Force Base (FL): Air Force Armament Laboratory (US); 1981 Oct. Report No.: AFATL-TR-81-87.

40. West KO, Whyte RH. Free flight and wind tunnel test of a missile configuration at subsonic and transonic Mach numbers with angles of attack up to 30 degrees. Proceedings of the 11th Navy Aeroballistic Symposium; 1978 Aug.

41. Jenke LM. Experimental roll-damping, Magnus, and static-stability characteristics of two slender missile configurations at high angles of attack (0–90 deg) and Mach numbers 0.2 through 2.5. Arnold Air Force Base (TN): Arnold Engineering and Development Center (US); 1976 July. Report No: AEDC-TR-76-58.

42. Bhagwandin,V. High-alpha prediction of roll damping and Magnus stability coefficients for finned projectiles. Journal of Spacecraft and Rockets. 2016 July-Aug;54:720–729.

43. Bhagwandin V, Sahu J. Numerical prediction of pitch damping stability derivative for finned projectiles. Journal of Spacecraft and Rockets. 2014 Sep-Oct;51:1603–1618.

44. Reinecke WG. Aerodynamic coefficients for extending and bending projectiles. Proceedings of the 23rd International Symposium on Ballistics; 2007 Apr; Tarragona, Spain.

45. Rosema C. Doyle J. Blake W. Missile DATCOM user's manual – 2014 revision. Wright Patterson Air Force Base (OH): Air Force Research Laboratory (US); 2014 Dec. Technical Report No.: AFRL-RQ-WP-TR-2014-0281.

46. Metacomp. Agoura Hills (CA): Metacomp Technologies Inc [accessed 2016 Aug 2]. http://www.metacomptech.com/index.php/products/cfd.

47. Sahu J, Heavey K, Time-accurate computations for rapid generation of missile aerodynamics. Proceedings of the AIAA Atmospheric Flight Mechanics Conference; 2010 Aug. Paper No.: AIAA-2010-8248.

48. Aftosmis MJ, Berger MJ, Adomavicius G. A parallel multilevel method for adaptively refined Cartesian grids with embedded boundaries. Proceedings of the 38th Aerospace Sciences Meeting and Exhibit; 2000. Paper No.: AIAA 2000-0808.

49. Aftosmis MJ, Nemec M, Cliff SE. Adjoint-based low-boom design with Cart3D. Proceedings of the 29th AIAA Applied Aerodynamics Conference; 2011 June; Honolulu, HI. Paper No.: AIAA 2011-3500

50. Smith SC, Nemec M, Krist SE. Integrated nacelle-wing shape optimization for an ultra-high bypass fanjet installation on a single-aisle transport configuration. Proceedings of the 51st AIAA Aerospace Sciences Meeting/New Horizons Forum and Aerospace Exposition; 2013. Paper No.: AIAA 2013-0543

51. Rodriguez D. Response surface based optimization with a Cartesian CFD method. Proceedings of the 41st Aerospace Sciences Meeting and Exhibit; 2003 Jan. Paper No.: AIAA 2003-0465

52. Dassault Systems SolidWorks Corporation. SolidWorks 2016. www.solidworks.com.

53. Auman LM, Kirby-Brown K. MissileLab user's guide. Redstone Arsenal (AL): Army Aviation and Missile Research, Development and Engineering Center (US); 2012 Oct. Technical Report No.: RDMR-SS-12-08.

54. MATLAB 9.0, The MathWorks, Inc. www.mathworks.com.

Nomenclature

α	angle of attack, degrees
C_D	drag coefficient
C_L	lift coefficient
C_m	pitching moment coefficient
C_{m_0}	pitching moment coefficient at zero degrees angle of attack
C_p	pressure coefficient
c.g.	projectile center-of-gravity, millimeters
D	projectile diameter, millimeters
f	objective function score
H	hypotenuse, millimeters
L/D	lift-to-drag ratio
n	swarm size
Q_l	hinge location relative to center of gravity, millimeters
$\bar{q}$	dynamic pressure
δ	canard deflection angle, degrees
Φ_1	nose bend angle, degrees
Φ_2	body bend angle, degrees
Θ	cumulative angle, degrees

List of Symbols, Abbreviations, and Acronyms

3-D	three-dimensional
AFF	Air Force Finner
CFD	computational fluid dynamic
PSO	Particle Swarm Optimization
RANS	Reynolds-Averaged Navier–Stokes
STL	stereolithography

1 (PDF)	DEFENSE TECHNICAL INFORMATION CTR DTIC OCA
1 (PDF)	CCDC ARL FCDD RLD CL TECH LIB
1 (PDF)	GOVT PRINTG OFC A MALHOTRA
1 (PDF)	CCDC ARL FCDD RLW LE J PAUL